Key Points:
- Lateral variations in lower crustal strength provide a first-order control on the shape and temporal evolution of mountain ranges
- Strong lower crust in the Sichuan Basin can explain the development of topography in the Longmen Shan without a lower crustal channel
- Lateral transport of samples should be considered in interpreting palaeoelevations from stable-isotope palaeoaltimetry

Correspondence to:
C. Penney,
cp451@cam.ac.uk

Lateral Variations in Lower Crustal Strength Control the Temporal Evolution of Mountain Ranges: Examples From South-East Tibet

Camilla Penney[1] and **Alex Copley[1]**

[1]COMET, Bullard Laboratories, University of Cambridge, Cambridge, UK

Abstract Controversy surrounds the rheology of the continental lithosphere, and how this rheology controls the evolution and behavior of mountain ranges. In this study, we investigate the effect of lateral contrasts in the strength of the lower crust, such as those between cratonic continental interiors and weaker rocks in the adjacent deforming regions, on the evolution of topography. We combine numerical modeling with recently published results from stable-isotope palaeoaltimetry in south-east Tibet. Stable-isotope palaeoaltimetry in this region provides constraints on vertical motions, which are required to distinguish between competing models for lithosphere rheology and deformation. We use numerical modeling to investigate the effect of lateral strength contrasts on the shape and temporal evolution of mountain ranges. In combination with palaeoaltimetry results, our modeling suggests that lateral strength contrasts provide a first-order control on the evolution of topography in south-east Tibet. We find that the evolution of topography in the presence of such strength contrasts leads to laterally varying topographic gradients, and to key features of the GPS- and earthquake-derived strain-rate field, without the need for a low-viscosity, lower-crustal channel. We also find that palaeoaltimetric samples may have been transported laterally for hundreds of kilometers, an effect which should be accounted for in their interpretation. Our results are likely to be applicable to the evolution of mountain ranges in general and provide an explanation for the spatial correlation between cratonic lowland regions and steep mountain range-fronts.

Plain Language Summary The rocks which make up the Earth's continents move and change shape in response to tectonic forces. How rocks respond to these forces depends on their material properties, which can vary in space and time. These material properties, therefore, control the shape of mountain ranges, and how mountains grow. This study investigates why some mountain ranges have steep fronts, while others have gentle gradients. We look at how regions made up of strong rocks (such as the Sichuan Basin) affect the shape and growth of adjacent mountain ranges. We find that mountain ranges with steep fronts can form when weaker rocks move over stronger ones. Recent measurements of oxygen in ancient soils suggests that parts of the south-eastern margin of the Tibetan Plateau (between the Sichuan Basin and the Central Lowlands of Myanmar) have been high since about 50 million years ago, and that the area has risen more slowly than has previously been estimated. In south-east Tibet, the pattern of earthquakes, and how fast the mountains have grown, can be explained by these strong areas, without invoking complicated material properties in the mountain ranges. Such strong regions may be important in controlling the shape of mountain ranges globally.

1. Introduction

The strength of the lithosphere provides a first-order control on the distribution of strain within it. Strength, here, means resistance to deformation, which might be controlled by the stresses transmitted across faults in the brittle part of the lithosphere or the rheology associated with ductile creep in the mid-to-lower crust and upper mantle. Lateral strength contrasts, such as those between cratonic continental interiors made of cool, anhydrous rocks (from which volatiles have been removed by previous partial melting) and the adjacent deforming regions made of hotter and more hydrous rocks, are a feature of continental lithosphere globally. Such contrasts control the distribution of strain in the continents and, therefore, the evolution of mountain ranges (e.g., England & Houseman, 1985; Flesch et al., 2001; Jackson et al., 2008; Vilotte et al., 1984). Regions with strong crust, such as cratons, tend to accommodate little strain in comparison to

their surroundings. In the India-Eurasia collision, for example, it is the accreted terranes which form the southern margin of Eurasia, rather than cratonic India, which have accommodated most of the shortening. Here we investigate the effect of lateral contrasts in the strength of the lower crust on the temporal evolution of mountain belts.

A key outstanding question about the effect of lateral strength contrasts is how regions with strong lower crust, and the flow of less viscous material over and around them, affect the evolution of mountain ranges over tens of millions of years. Previous studies of continental deformation demonstrate that models which are able to reproduce instantaneous strain rates do not necessarily lead to the formation of the observed topography over time (e.g., England & Houseman, 1986; Houseman & England, 1986), so incorporating temporal evolution is an important extension to models considering the geologically instantaneous effects of strength contrasts (e.g., Bischoff & Flesch, 2019; Copley, 2008). This study concerns the physical controls on mountain building, and the constraints which recently published stable-isotope palaeoaltimetry observations can provide on lithosphere rheology. Vertical motions, to which palaeoaltimetry observations are sensitive, have the potential to distinguish between rheological models which lead to the same horizontal surface velocities (Copley, 2008; Flesch et al., 2018). Understanding the implications of these observations, and the associated caveats is, therefore, critical to constraining lithosphere rheology. Numerical models with a small number of parameters allow us to test whether lower-crustal strength contrasts, consistent with geological and geodetic observations, can reproduce lateral variations in topographic gradients, or whether other driving mechanisms are required. In this study, we combine recently published palaeoaltimetry observations from south-east Tibet with a simple 3D model of crustal deformation, to explore the effects of lateral strength contrasts on continental deformation.

The south-eastern margin of the Tibetan plateau (here referred to as "south-east Tibet" Figure 1) is a good place to study the effect of lateral strength contrasts. Low elevations, relief and strain rates (both seismic — Figure 1 — and geodetic — Maurin et al., 2010; Zheng et al., 2017) in the Sichuan Basin and the Central Lowlands of Myanmar suggest that these regions experience relatively little deformation. These regions are, therefore, likely to be strong in comparison to the high region between them, and the mountain belts which surround them, which have undergone significant recent and cumulative deformation. The Sichuan Basin is covered by ~10 km of sediments (Hubbard & Shaw, 2009), underlain by Paleoproterozoic crust (Burchfiel et al., 1995) with high seismic velocities in the upper mantle (e.g., Lebedev & Nolet, 2003; Li and Van Der Hilst, 2010). Postseismic motion after the 2008 Wenchuan earthquake suggests a strength contrast across the Longmen Shan (Huang et al., 2014), as do differences in elastic thickness between the Longmen Shan and the Sichuan Basin, estimated from gravity anomalies (Fielding & McKenzie, 2012).

Although the Central Lowlands of Myanmar have been less extensively studied than the Longmen Shan, the lack of topography, and the presence of undeformed Miocene sediments suggest low rates of post-Miocene deformation (Wang et al., 2014). Initial GPS measurements by Maurin et al. (2010) suggest that central Myanmar, west of the Sagaing fault, deforms in a coherent manner. Earthquakes in the Central Lowlands of Myanmar, shown in Figure 1b, are associated either with strike-slip motion on the Sagaing fault, on the eastern margin of the lowlands (which accommodates a component of the oblique India-Eurasia convergence; Maurin et al., 2010), or with active subduction beneath the Indo-Burman ranges (e.g., Steckler et al., 2016; Stork et al., 2008. Yellow focal mechanisms in Figure 1b have depths >50 km). The seismic strain rate within the Central Lowlands is, therefore, low, at least in the instrumental period.

In contrast, the high regions of south-east Tibet deform rapidly, with kinematics described in detail by Copley (2008), who also summarized the work of previous authors. Since that study, numerous thrust-faulting earthquakes have occurred along the Longmen Shan, including the 2008 Wenchuan and 2013 Lushan earthquakes and their aftershocks (Figure 1). These earthquakes, and subsequent analysis of shortening on structures imaged in seismic profiles (Hubbard & Shaw, 2009), demonstrate that active shortening of the brittle upper crust is occurring across the Longmen Shan.

Much of the morphology of south-east Tibet is dominated by deeply incised river valleys, often following strike-slip faults (Wang and Burchfiel, 1997). Collectively these strike-slip faults accommodate south-eastwards motion of high topography relative to both the Sichuan Basin and the Central Lowlands of Myanmar (e.g., Shen et al., 2005), with the faults on opposite sides of the high region accommodating opposite senses
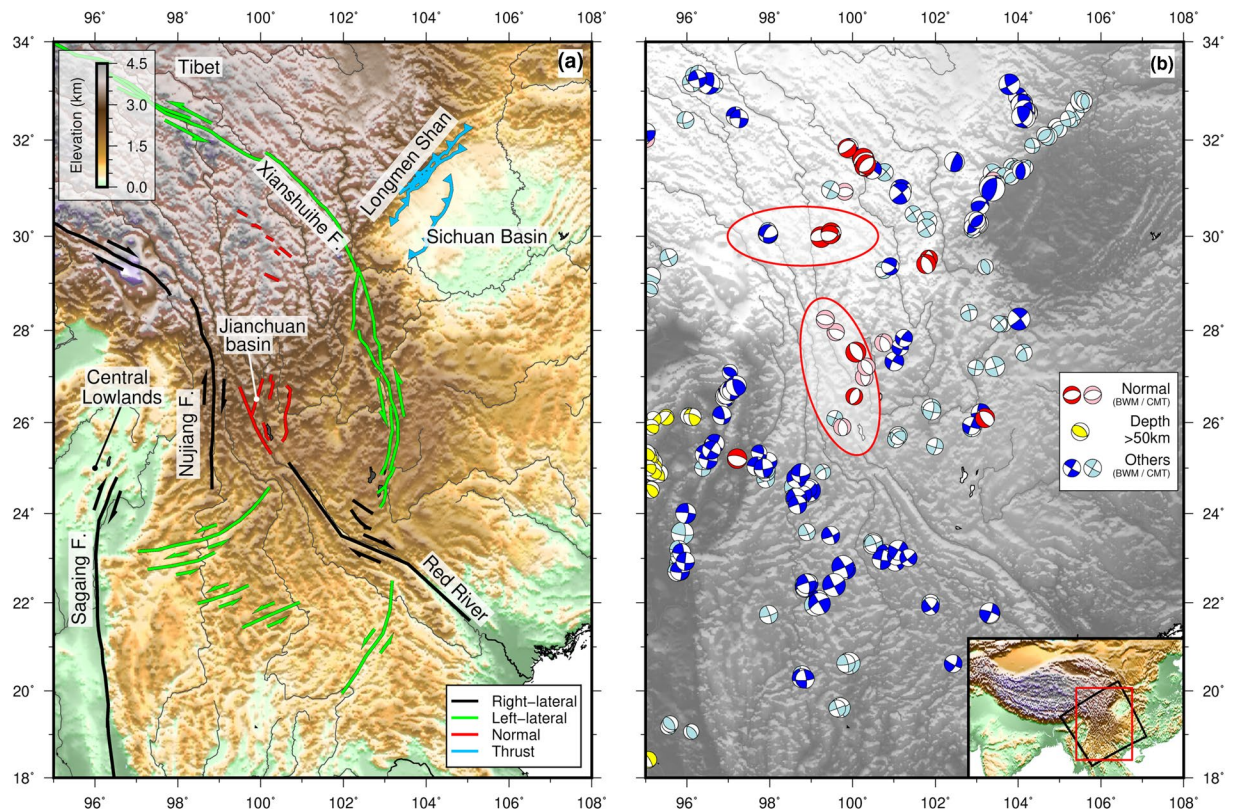
Figure 1. (a) Major active faults in south-east Tibet, from Copley (2008); Hubbard and Shaw (2009) and references therein. Black and green lines are right- and left-lateral strike-slip faults respectively. Note the opposite sense of shear adjacent to the Central Lowlands of Myanmar and Sichuan Basin. Red lines show normal faults. Blue lines show thrust faults with teeth on the hanging-wall side. (b) Focal mechanisms of earthquakes in south-east Tibet. Focal mechanisms determined from body-waveform modeling from Copley (2008) (and references therein), Zhang et al. (2010), Z. Li et al. (2011), Han et al. (2014), Bai et al. (2017), Han et al. (2018) are shown in red if they have a rake of −90 ± 35° (normal faulting), and dark blue otherwise. Yellow focal mechanisms are > 50 km deep and are associated with subduction beneath the Indo-Burman ranges, most other earthquakes have depths less than ~20 km. Focal mechanisms in pink (normal faulting, with rakes of −90 ± 35°) and pale blue are those from the CMT catalog up to May 2016 with >70% double couple and >10 depth phases in the EHB catalog if the earthquake occurred before 2009. Two regions of normal faulting discussed in the text are circled in red. Red box in inset shows the figure's location, black box shows location of Figure 3.

of shear (Figure 1a). The Xianshuihe and Sagaing faults (Figure 1a) have left- and right-lateral geodetic slip rates of ~7–9 mm yr^{-1} and ~18 mm yr^{-1} respectively (Maurin et al., 2010; Zheng et al., 2017). The region of distributed left-lateral faulting east of the Sagaing fault (Figure 1a) accommodates right-lateral shear on north-south striking planes through rotations about vertical axes (Copley, 2008).

A suite of models (e.g., Burchfiel et al., 2008; Clark, Bush, & Royden, 2005; Clark & Royden, 2000; Royden et al., 1997) have focused on the possibility of flow in a low viscosity, lower-crustal channel as an explanation for the steep topography of the Longmen Shan and the gentle topographic gradients to the south of the basin. By extending these channel-flow models to include rigid regions, Cook and Royden (2008) argued for the importance of both a strong Sichuan Basin, and flow in a mid-lower crustal channel in the formation of steep topography across the Longmen Shan. Chen, Gerya, Zhang, Zhu, et al. (2013) and Chen, Gerya, Zhang, Aitken, et al. (2013) used 2D thermo-mechanical models with extrapolated laboratory flow laws to demonstrate that the craton was an important control on deformation in the region. We build upon this work by using a simple 3D model to isolate the effects of this rigid, cratonic region, and by comparing the results to observational constraints from palaeoaltimetry.

Vertical velocities can distinguish between competing models of depth-dependent rheology which would lead to the same horizontal velocities (Bischoff & Flesch, 2019; Copley, 2008; Flesch et al., 2018). Copley (2008) demonstrated that rapid flow at depth associated with a weak mid-to-lower crust in the Longmen Shan would lead to faster instantaneous vertical motions than coherent upper- and lower- crustal

deformation. The specific rates were based on instantaneous calculations, so would not necessarily apply to the geologically recorded uplift rates, but exemplify the possibility of using vertical motions to distinguish between different models of depth-dependent rheology.

Many quantitative studies of topographic evolution in south-east Tibet have focused on thermochronology (e.g., Clark et al., 2004; Kirby et al., 2002; E. Wang et al., 2012, 2016). Thermochronometric ages give information about exhumation, which is controlled by the interplay between tectonics and erosion. Such ages have been interpreted to imply that rapid uplift occurred ∼13–5 Ma, based on the identification of geomorphic surfaces presumed to have formed at low elevation (Clark, Bush, & Royden, 2005; Clark et al., 2006). However, it has been suggested that such low-relief, erosional surfaces can also form at high elevations (e.g., Liu-Zeng et al., 2008; Yang et al., 2015) and that increased exhumation may have been related to changes in the base level of rivers draining the region rather than tectonic uplift (e.g., Richardson et al., 2008). The interpretation of the existing thermochronometric data in terms of elevation history is therefore unclear. In this study we make use of recently published estimates of palaeoelevation from stable-isotope geochemistry, which provide an opportunity to quantitatively constrain the elevation history of south-east Tibet and, therefore, to distinguish between competing models of lithosphere rheology and mountain-range evolution.

We first summarize recently published results from stable-isotope palaeoaltimetry (Section 2) to constrain the uplift and elevation history of south-east Tibet. We then use fluid-dynamical modeling of the mountain range (described in Section 3) to investigate the effects of lateral strength contrasts on the evolution of topography through time, and compare our results to south-east Tibet (Section 4).

Although the results presented here are in the context of south-east Tibet, the presence of lateral strength contrasts is a common feature of mountain ranges globally (e.g., Dayem, Houseman, & Molnar, 2009; Dayem, Molnar, et al., 2009; Jackson et al., 2008; Lamb, 2000; Nissen et al., 2011). In particular, many mountain ranges, both active and older, have edges adjacent to cratons (e.g., McKenzie & Priestley, 2008); regions of (often thick) continental lithosphere, usually composed of Proterozoic or Archean crust, which have remained relatively undeformed by tectonic events on their margins (Holmes, 1965). In Section 5, therefore, we discuss the applicability of our results to the temporal evolution of mountain ranges in general.

2. Palaeoaltimetry

Stable-isotope palaeoaltimetry uses systematic variations in the isotopic composition of precipitation (usually $\delta^{18}O$) with elevation to derive the palaeoelevation of sample sites (e.g., Rowley et al., 2001). These techniques have been developed in order to place quantitative constraints on the elevation history of orogenies, such as Tibet, but they have not yet been extensively used as a constraint in dynamic models.

South-east Tibet is a good region to carry out palaeoaltimetry studies. Moisture paths from the ocean to high topography in this region are simple, as shown by the Rayleigh fractionation relationship between the oxygen-isotope composition of precipitation and elevation in present-day elevation transects (Hren et al., 2009).

Figure 2 shows results from seven recent palaeoaltimetry studies in south-east Tibet, which use soil-deposited (Gourbet et al., 2017; Hoke et al., 2014; Tang et al., 2017; Xiong et al., 2020; Q. Xu et al., 2016) and/or lacustrine (Gourbet et al., 2017; S. Li et al., 2015; Wu et al., 2018; Q. Xu et al., 2016) carbonates to derive the oxygen-isotope composition of palaeo-precipitation and, hence, palaeoelevations. In south-east Tibet, the age of sampled formations is a significant source of uncertainty (Hoke, 2018). Gourbet et al. (2017) and S. Li et al. (2020) have recently revised the ages of formations in the Jianchuan and Lühe basins respectively (Figure 2b). In the most extreme cases, the revised dating has shown that formations previously mapped as mid-to-late Miocene were deposited in the late Eocene (Gourbet et al., 2017). Hotter global temperatures in the Eocene (Miller et al., 1987; Savin, 1977; Zachos et al., 2001) alter the relationship between isotopic composition and elevation, resulting in multiple palaeoelevation estimates for some samples, depending on which relationships were used (filled and unfilled symbols in Figure 2b show palaeoelevation estimates calculated using modern and Eocene relationships respectively). However, the differences in palaeoelevation resulting from whether hotter temperatures are used are generally much less than the kilometer scale of
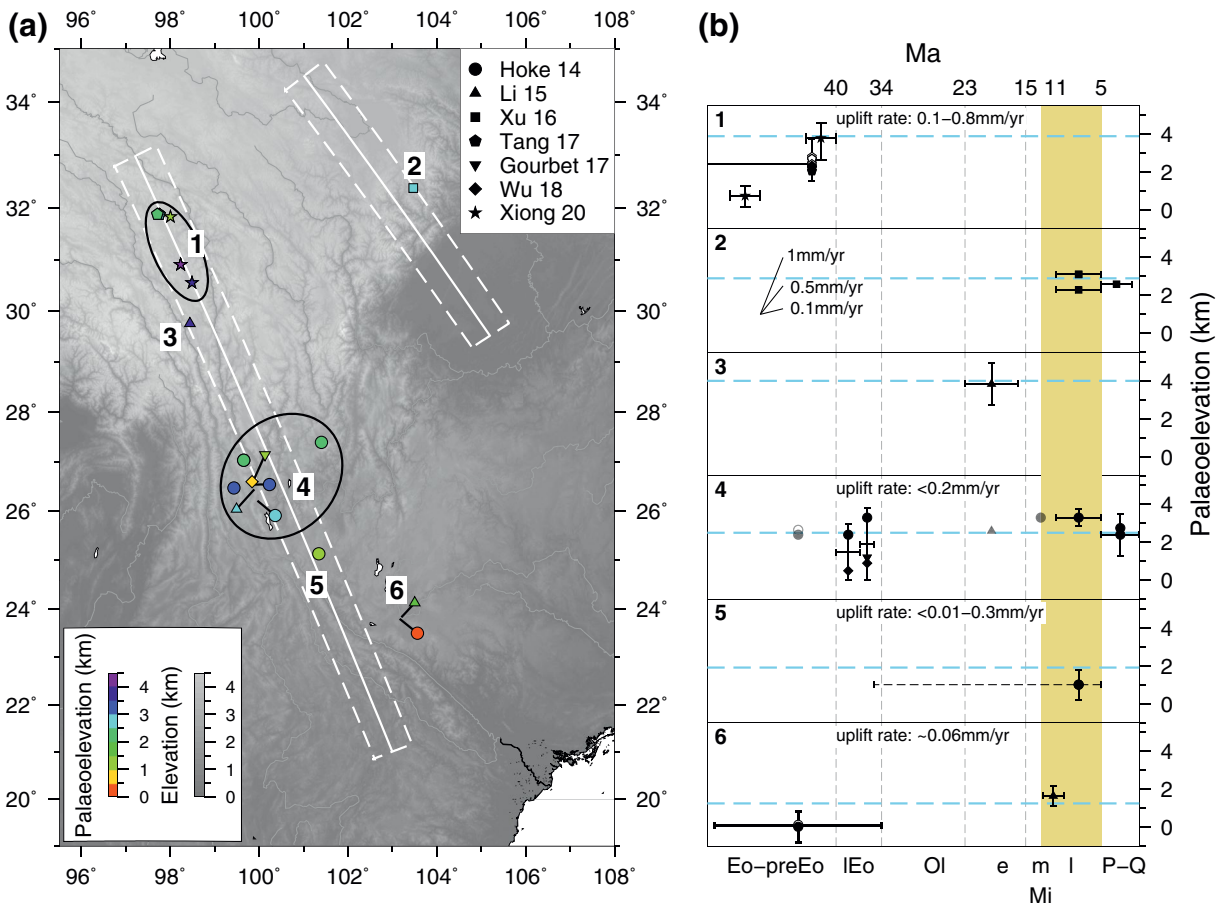
Figure 2. Results of stable-isotope palaeoaltimetry studies in south-east Tibet. (a) Sample localities from Hoke et al. (2014); S. Li et al. (2015); Q. Xu et al. (2016); Tang et al. (2017); Gourbet et al. (2017), Wu et al. (2018) and Xiong et al. (2020) are colored by palaeoelevation. Six regions are labeled, which correspond to panels in b, ellipses indicate the extents of regions 1 (Gonjo Basin) & 4 (Jianchuan and surrounding basins). White lines and boxes show the regions plotted as topographic profiles in Figures 6g and 6h. (b) Sample ages and palaeoelevations in each region. Epoch labels are—Eo-preEo: Eocene-pre Eocene >40 Ma, lEo: late Eocene: 40–34 Ma, Ol: Oligocene 34–23 Ma, eMi: early Miocene 23–15 Ma, mMi: middle Miocene 15–11 Ma, lMi: late Miocene 7–5 Ma, P–Q: Pliocene–Quaternary 5–0 Ma. Symbol shapes are as in (a). Yellow bar shows the timing of increased exhumation and erosion rates suggested by Clark, House, et al. (2005) to indicate rapid uplift. Dashed blue lines indicate mean present-day sample-site elevation for each region. Where multiple samples from the same author are reported in the same epoch in the same region only a single error bar (representing the highest and lowest palaeoelevation estimates) is plotted. Palaeoelevation estimates using a modern temperature-elevation relationship are shown as filled symbols, those using a higher Eocene temperature estimate are unfilled. Gray points in region 4 are the authors' original palaeoelevation/age inferences. Black points in region 4 show the revised palaeoelevations/ages from Gourbet et al. (2017) and Wu et al. (2018), which we use to determine uplift rates. The age error bar in region 5 indicates the reassessment of S. Li et al. (2020)—those authors did not recalculate the paleoelevation of the sample based on the revised dating.

interest for dynamic modeling, even for upper-bound estimates of Eocene temperature (region 4, Figure 2b, Hoke et al., 2014; S. Li et al., 2015; Tang et al., 2017; Wu et al., 2018).

The oxygen-isotope ratio at sea level is also time-dependent. Licht et al. (2014) found very negative values of $\delta^{18}O$ in an Eocene gastropod and rhinoceroid from Myanmar, taken as sea level references for the time. Preliminary results from isotopic analysis of soil-deposited carbonates in the same area show similarly low $\delta^{18}O$ (Licht et al., 2019). A more negative starting value leads to lower palaeoelevation estimates, since Rayleigh fractionation predicts increasingly negative $\delta^{18}O$ with elevation. These improved estimates of sea-level composition, as well as the dating discussed above, have led to recalculations of palaeoelevation in south-east Tibet (Gourbet et al., 2017; Wu et al., 2018, shown as black symbols in Figures 2b–4, the original estimates are shown in gray), and we use these in our uplift rate calculations.

Uplift rates can be derived from stable-isotope palaeoaltimetry if samples can be taken from rocks of multiple ages at the same location or compared with the present-day elevation (blue dashed lines in Figure 2b).
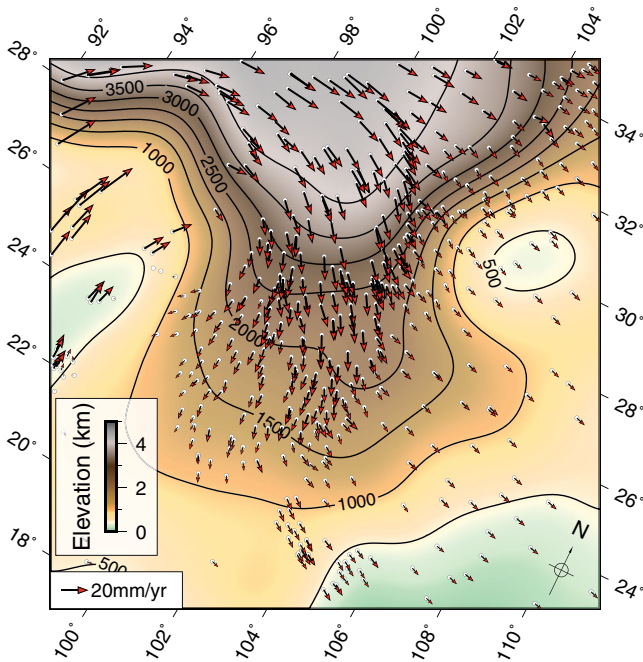
Figure 3. Topography of south-east Tibet after applying a low-pass 500 km-diameter Gaussian filter in an oblique Mercator projection (equator azimuth 60°, centered on 101.5°E, 26.5°N, location shown as black box in the inset of Figure 1b) for comparison to our model set-up (Figure 4) and results (Figures 5 and 8, Section 4). GPS velocities from Zheng et al. (2017) are shown in a Eurasia-fixed reference frame.

These rates, therefore, only reflect points in space and time which are preserved in the carbonate record. Where such rates can be inferred they are shown in Figure 2b. All but one of these inferred uplift rates are <0.3 mm yr^{-1}.

In most of the regions shown in Figure 2, paleoelevations similar to present-day elevations are found in the oldest sampled formations. To the north-west (region 1), Tang et al. (2017) suggest that topography may have been high since before the Eocene. Xiong et al. (2020) also found high topography in the Gonjo basin by the late Eocene, though their results suggest that this uplift may have occurred during the Eocene, giving possible early Eocene uplift rates of up to 0.8 mm yr^{-1}, the only uplift rate >0.3 mm yr^{-1} in the studies reviewed here. Although Q. Xu et al. (2016)'s measurements have significant uncertainty in the moisture source, they suggest a lower bound for the elevation of the Longmen Shan in the late Miocene of ~3,000 m, compared to present-day elevations of 2,800–3,700 m. To the south-east, region 5 may have experienced some uplift since the late Miocene, at rates <0.3 mm yr^{-1}, and region 6 is likely to have been at its present elevation by the late Miocene.

These stable-isotope palaeoaltimetry results suggest that at least some areas of present-day south-east Tibet have been high since the late Eocene, and are likely to have reached present-day elevations prior to the onset of rapid exhumation inferred by Clark, House, et al. (2005) from the incision of river gorges (gray region in Figure 2b). Uplift rates across south-east Tibet are likely to have been much lower (<0.3 mm yr^{-1}) than would be predicted if all the topographic growth in the region had occurred since the late Miocene. Recently published thermochronology is also consistent with this palaeoaltimetric data, suggesting that topography across the Longmen Shan had begun to develop by the Oligocene (E. Wang et al., 2012), and that uplift may have been ongoing since the Paleocene (Liu-Zeng et al., 2018).
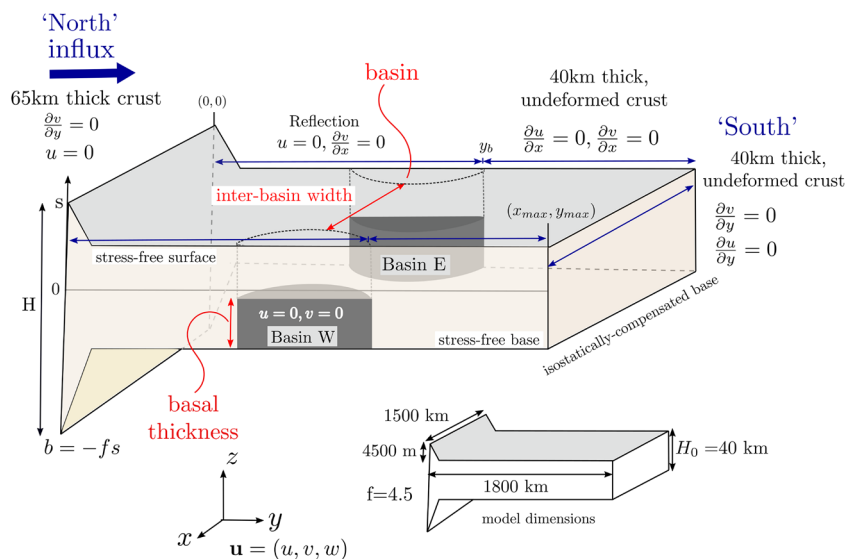
Figure 4. Model geometry, showing the initial topography and symmetric rigid regions. Boundary conditions on $x = x_{\max}$ are the same as those on $x = 0$. Inset shows dimensions of model domain. The isostatic root is not shown to scale.

3. Dynamical Modeling

In tandem with the palaeoaltimetry estimates summarized in Section 2, we use numerical modeling to investigate the effect of lateral contrasts in lower crustal strength on the temporal evolution of mountain ranges. We first summarize the work of previous authors (Section 3.1) and then describe the setup for the model used here (Section 3.2) and our boundary conditions (Section 3.3), before describing the model results in Section 4. Our model is designed to investigate the first-order effects of lateral strength contrasts on the multi-million-year development of long-wavelength topography in general, rather than to simulate the detailed evolution of south-east Tibet.

3.1. Previous Models

In regions of distributed deformation, the continental lithosphere can be modeled as a continuum (commonly a viscous fluid), with motion driven by horizontal pressure gradients — resulting from gravity acting on elevation contrasts — and by the relative motion of the bounding plates (e.g., England & McKenzie, 1982, 1983; Flesch et al., 2001; Flesch et al., 2018; Houseman & England, 1986; Lamb, 2000; Reynolds et al., 2015; Royden et al., 1997). Many authors use the thin-viscous-sheet model, which assumes negligible depth variations in horizontal velocities (England & McKenzie, 1982, 1983). This model implicitly assumes that the top and base of the lithosphere experience shear tractions which are small in comparison to normal components of the deviatoric stress tensor (here referred to as a stress-free basal boundary condition, after McKenzie et al., 2000). In the thin-viscous-sheet model, this corresponds to flow over a less viscous fluid (the asthenosphere). Such models can only produce steep-fronted topography if the lithosphere has an effective power-law rheology with a high stress exponent (typically greater than 3, i.e., shear-thinning, e.g., Houseman & England, 1986; Lechmann et al., 2011). The typical topographic gradients produced by these models are still much less steep than those in steep-fronted mountain ranges such as the Himalayas and the Longmen Shan (England & Houseman, 1986). Geologically, stress exponents greater than 1 are associated with rocks deforming by dislocation creep (e.g., Stocker & Ashby, 1973, discussed further in Section 5).

Steep topographic gradients often occur adjacent to lateral contrasts in lithosphere strength. Such regions are commonly associated with large gradients in crustal thickness, and, if less viscous material flows over a much higher viscosity region, this is equivalent to flow over a rigid base (referred to here as a no-slip basal boundary condition, defined as zero-horizontal velocity after McKenzie et al., 2000). In such regions the thin-viscous-sheet approximation breaks down, because flow over a rigid base is accommodated by vertical gradients of horizontal velocity in the flowing layer. Medvedev and Podladchikov (1999a) presented an extension to the thin-viscous-sheet model to allow for rapid spatial variations in material properties, which was applied to 2D geodynamic scenarios by Medvedev and Podladchikov (1999b). An alternative approach is to use full thermo-mechanical models in either 2D (e.g., Beaumont et al., 2001) or 3D (e.g., Lechmann et al., 2011; Pusok & Kaus, 2015). Here we discuss a simplified approach, which allows us to incorporate flow over both stress-free and rigid boundaries into a single 3D model with a small number of adjustable parameters.

Previous studies incorporating vertical gradients of horizontal velocity have focused on reproducing geologically instantaneous deformation in south-east Tibet (e.g., Bischoff & Flesch, 2019; Copley, 2008; Lechmann et al., 2014). These studies have demonstrated that key features of the instantaneous earthquake- and GPS-derived velocity field can be explained by lateral viscosity contrasts between cratonic blocks and the surrounding mountain ranges. Studies which have investigated the effects of these cratonic blocks on the temporal evolution of topography in south-east Tibet have used complex models at the scale of entire collision zones (e.g., Pusok & Kaus, 2015), or imposed external forcing or velocities to drive the flow (e.g., Cook & Royden, 2008). Here, we use a simple model of 3D crustal deformation, described below, to isolate the effects of lateral strength contrasts on the evolution of topography through time. Our interest is in understanding the physical controls on topographic evolution, in particular the development of laterally contrasting topographic gradients. Consideration of the temporal evolution of the topography is important because it allows us to investigate the constraints which can be provided by the newly available palaeoaltimetry data.

3.2. Model Setup

We model the lithosphere as a viscous fluid. The geometry and boundary conditions we use are based on the long-wavelength topography of south-east Tibet (Figure 3). Using a geometry similar to south-east Tibet allows us to make use of the palaeoaltimetric results described in Section 2 in assessing the uplift rates in the model.

GPS velocities (relative to Eurasia) in south-east Tibet are subparallel to topographic gradients (Figure 3). Movement of material along topographic gradients suggests that the deformation in south-east Tibet is governed by gravitational potential energy gradients. The models we investigate here are, therefore, driven by gravity acting on crustal thickness contrasts, without applied compressive forces or imposed boundary velocities. This category of models has been described by Lechmann et al. (2014) as "density driven." Analogous models have been applied since the 1980s to the gravitational spreading of crustal thrust sheets (e.g., Merle & Guillier, 1989; Ramberg, 1981). Here we consider deformation on the lithosphere scale, rather than the lengthscale of individual thrust sheets. These earlier studies also considered analogs between glaciological and geological gravity-driven deformation, including the possibility of both stress-free and no-slip basal boundary conditions (Ramberg, 1981). We extend this analogy here by using methods developed for ice-sheet modeling to solve the governing equations.

We solve a simplified form of the Stokes′ equations using the method proposed by Pattyn (2003), which includes vertical gradients of horizontal velocities. This method allows us to model flow over a stress-free base and also a no-slip base, representing regions of strong lower crust, unlike traditional thin-viscous-sheet models (England & McKenzie, 1982, 1983). The implementation and more mathematical details of this approach are given in Appendix A.

The method we use here has previously been used to calculate instantaneous strain rates in south-east Tibet (Copley, 2008). Reynolds et al. (2015) extended this approach to model the temporal evolution of the Sulaiman Ranges by re-writing the incompressibility condition as a diffusion equation for topography (Pattyn, 2003). We use an improved method (Appendix A) to solve this diffusion equation, calculating diffusivities on a staggered grid, and using the generalized minimum residual method (Saad & Schultz, 1986) to solve the resulting sparse matrix equations. We use a regular horizontal grid of 15×15 km, and 20 grid points in the vertical, which are re-scaled at each time step (Appendix A; Pattyn, 2003). The assumptions and set-up of this model are discussed below.

We model the deforming crust as an isoviscous, Newtonian fluid. Using a simple rheology allows us to test the extent to which topographic evolution in south-east Tibet is controlled by the presence of lateral lower crustal strength contrasts, and whether additional rheological complexity is required to explain the geophysical and geological observations. The simple rheology we use contrasts with the approach of previous authors studying the effect of a strong craton on the evolution of topography in south-east Tibet. For example, Chen, Gerya, Zhang, Zhu, et al. (2013) used a 2D model with multiple rock types and an assumed geotherm. Cook and Royden (2008) included a weak lower crustal channel and drove deformation within their model through an imposed velocity at its base. By using a simpler rheology, we are able to isolate the effects of lower crustal strength contrasts on the evolution of topography. We discuss the possible effects of a more complicated rheology in Section 5. The equations relating velocities in the fluid to gradients in topography are linearly dependent on the fluid viscosity (Appendix A) so although we use a viscosity of 10^{22} Pas here (as suggested for south-east Tibet by Copley & McKenzie, 2007), we expect that these models will apply to different viscosities with scaled times and velocities. For example, we expect the topography after 50 Myr of model evolution with a viscosity of 10^{22} Pas to be the same as that after 5 Myr for a viscosity of 10^{21} Pas. The velocities would be 10 times greater in the 10^{21} Pas case.

We impose Airy isostatic compensation at the base of the crust, relative to a column of mantle (Flesch et al., 2001), with crust and mantle densities $\rho_c = 2,700$ kg m^{-3} and $\rho_m = 3,300$ kg m^{-3} respectively, giving a ratio of crustal-root depth to topographic elevation of 4.5 (f in Figure 4). Assuming Airy isostatic compensation neglects flexural support of the topography. By using a viscous model, we are implicitly considering long-wavelength deformation (motivated by the long-wavelength shape of the topography in Figure 3). Free-air gravity anomalies from south-east Tibet (Fielding & McKenzie, 2012) suggest that flexure plays a role in supporting the topography on relatively short wavelengths ($\sim$50 km into the Longmen Shan), which

means that isostatic compensation is an appropriate assumption throughout most of the model domain. At the edge of the basin region, where flexural support may be important, flexure would be expected to give a shape for the basal boundary that is intermediate between full isostatic compensation, which we use here, and a base which cannot move vertically in response to loading, a case which is often considered in the fluid dynamics literature (e.g., Huppert, 1982). The implications of assuming isostatic compensation are discussed in Section 4.

Figure 4 shows a diagram of our model setup. High viscosity regions, analogous to the strong lower crust of the Sichuan Basin and the Central Lowlands of Myanmar, are simulated by setting horizontal velocities to zero in part of the model with a specified thickness ("basal thickness," gray areas in Figure 4). Flow can occur over and around these rigid regions ("basins," Basin E and Basin W in Figure 4), which deform vertically according to Airy isostasic compensation. The basal thickness is equivalent to the thickness of strong lower crust. The Sichuan Basin is connected to the South China craton (e.g., Li & Van Der Hilst, 2010), which provides a resistive force, so the basins in our model are not advected with the flow. By setting velocities to zero in these basin regions, we are assuming that the lower crust in the Sichuan Basin and Central Lowlands of Myanmar has behaved rigidly over the 50 Myr of deformation which we model. This approach is supported by inferences of strong lower crust and upper mantle in the Sichuan Basin and Central Lowlands of Myanmar (Section 1; Huang et al., 2014; C. Li & Van Der Hilst, 2010). An estimate of the lower crustal viscosity required for our assumption of rigidity to hold true can be calculated from the gravitational potential energy contrast between the Longmen Shan and Sichuan Basin. The crustal thicknesses in the Longmen Shan and Sichuan Basin are 65 and 36–40 km respectively (e.g., Q. Y. Liu et al., 2014), with 4.5 km of elevation contrast. The horizontal force associated with these variations of crustal thickness can be estimated from variations of gravitational potential energy between the two columns of crust (both of which are in Airy isostatic equilibrium with a column of mantle, e.g., Artyushkov, 1973; Dalmayrac & Molnar, 1981; Molnar & Lyon-Caen, 1988; Molnar & Tapponnier, 1978), giving a maximum horizontal force of 7×10^{12} N m^{-1}, similar to that applied by Tibet on cratonic India (e.g., Copley et al., 2010; Molnar & Lyon-Caen, 1988). Assuming that this force is distributed uniformly with depth in the crust, this horizontal force results in a maximum deviatoric normal stress acting on the Sichuan Basin of ~120 MPa. This stress, and therefore the required viscosity, would be lower if any of the stress were supported by the mantle. If this topographic contrast has existed since 50 Mya (the effective start time of our model) then for the Sichuan Basin, which is ~300 km wide, to have deformed by less than one grid cell in our model (15 km), requires a strain rate in the lower crust less than 3.2×10^{-17} s^{-1}. In this scenario the viscosity of the crust in the Sichuan Basin would need to be greater than $\sim 4 \times 10^{24}$ Pas to remain undeformed by horizontal forces associated with gravitational potential energy contrasts. The viscosity required would be lower if the topographic contrast were supported for a shorter time. We can test whether this viscosity is reasonable using laboratory-derived flow laws. We use the dry flow laws for typical lower crustal minerals from Bystricky and Mackwell (2001) and Rybacki et al. (2006), and calculate the temperature corresponding to a viscosity of 4×10^{24} Pas at the Moho (36–40 km, Q. Y. Liu et al., 2014), assuming lithostatic pressure and a grain size of 1 mm. For both flow laws, the viscosity will be $\geq 4 \times 10^{24}$ Pas if the temperature is less than ~800–900°C. Moho temperatures in undeforming Precambrian crust are typically ~600°C (McKenzie et al., 2005), meaning that the viscosity required for the Sichuan Basin to behave rigidly on the timescales of our model is consistent with laboratory-derived flows laws. Rather than adding additional parameters to our model describing the rheology of the lower crust in the basins, we simply model the lower crust in the basins as rigid. As discussed in Section 1, the geological structure of the Central Myanmar Basin is less well constrained than that of the Sichuan Basin, but it also acts in a rigid manner, so for simplicity we make the same assumption there.

Outside the basins, the base of the current in our models is stress-free (meaning that vertical derivatives of horizontal velocities are zero at the base of the current; Copley & McKenzie, 2007; England & McKenzie, 1982, 1983), implying that the asthenosphere imposes negligible shear stress on the base of the lithosphere. Since we only model the deformation of the crust, we are assuming that the crust and lithospheric mantle deform coherently in the region with the stress-free base, and that shearing over the lithospheric mantle plays a limited role in the force balance of the lower crust. For this assumption to hold true, the lithospheric mantle should have a sufficiently low viscosity that dominant stress driving its motion is the deviatoric stress resulting from flow in the lower crust, rather than the stress imposed on vertical planes by shearing past the basins. From our modeling, the deviatoric strain rate in the center of the interbasin

region is $\sim 5 \times 10^{-16} \mathrm{s}^{-1}$, giving a deviatoric stress of 10 MPa in the lower crust, using a crustal viscosity of 10^{22} Pas. The shear strain rate on the basin margins is $\sim 3 \times 10^{-15} \mathrm{s}^{-1}$. For our assumption to hold, therefore, the viscosity of the lithospheric mantle should be $\ll 10^{21}$ Pas. Using the flow laws derived for wet olivine by Hirth and Kohlstedt (2003) with a grain size of 1 mm, 1.5 GPa pressure (lithostatic pressure at the Moho beneath ~ 55 km thick crust), 1 GPa water fugacity, and a strain rate of $10^{-16} \mathrm{s}^{-1}$, effective viscosities less than 10^{21} Pas correspond to temperatures above ~ 400–700°C (depending on whether deformation occurs by dislocation or diffusion creep). Effective viscosities less than 10^{19} Pas, such that the shear stress imposed on the lithospheric mantle at the basin margins would be two orders of magnitude less than the principal deviatoric stress in the lower crust, correspond to temperatures above ~ 800°C. These temperatures are consistent with temperature estimates from lithospheric mantle xenoliths in south-east Tibet (C. Z. Liu et al., 2013; Yu et al., 2010), suggesting that modeling crustal deformation with a stress-free base outside the basin regions is reasonable. Copley (2008) also demonstrated the possibility of coherent lower crust and lithospheric mantle deformation in south-east Tibet using rheologies extrapolated from laboratory flow laws. Although such extrapolations lead to vertical gradients in viscosity, in many cases these gradients, and the length-scales over which they occur, are insufficient to result in appreciable contrasts in horizontal velocities.

The top surface of the current in our models is stress-free throughout the model domain, representing the lack of significant tractions imposed by the atmosphere. We track particles on this surface, which move with the horizontal velocity at their location at each time step. These particles are analogous to the samples used in palaeoaltimetric studies.

In some models we investigate the interaction between erosion and propagation of the current by incorporating an erosive term;

$$\frac{\partial s}{\partial t} = -\kappa \left| \nabla s \right|, \tag{1}$$

where κ is a constant. Gradient-dependent erosion is suggested by higher erosion rates and greater cumulative erosion in the Longmen Shan than in the interior of the Sichuan Basin and Tibetan Plateau (Richardson et al., 2008). This erosive term has the same derivation as the classic Culling model (Culling, 1960), but assumes that eroded material is removed from the model domain. This assumption is consistent with Hubbard et al.'s (2010) proposal that sediment is transported away from the Sichuan basin by the Yangtze River.

3.3. Lateral Boundary Conditions

The mathematical details of the lateral boundary conditions we use in our models are given in Appendix A. Here we summarize these boundary conditions and explain their physical motivation. The intention of these models is to investigate the effects of variations in the strength of the lower crust on the temporal evolution of topography. In south-east Tibet, this evolution is likely to be driven by gravitational potential energy contrasts (see Section 3.2 above), so the aim of these boundary conditions is to approximate the features of south-east Tibet which lead to, and control, the topographic evolution: high topography and thick crust in the Tibetan Plateau, and thinner crust to the south-east. The boundary conditions we adopt are symmetric, and do not vary in the x ("east-west") direction, so "east-west" variations in the development of topography in our model must result from the lateral changes in basal boundary conditions.

Initially ($t = 0$), the domain is filled with a 40 km-thick layer of fluid (H_0, Figure 4), chosen to represent generic, undeformed continental crust. There may have been preexisting topography in south-east Tibet before the onset of Cenozoic deformation (Burchfiel et al., 1995; Hubbard et al., 2010). However, the shape of this topography is poorly constrained, so we assume an initially flat, uniform layer for simplicity.

At one edge of the model domain ($y = 0$) fluid flows into the region, analogous to the lateral growth of a mountain range, in this case from central Tibet into south-east Tibet. The topography along this boundary is 4.5 km above the surface of the 40 km thick layer in the remainder of the model domain, similar to the mean elevation of the Tibetan Plateau above the Sichuan Basin (Figure 1). This elevation contrast, combined with our assumption of Airy isostasy, corresponds to a crustal thickness at the input boundary of 65 km,

similar to that beneath the Tibetan Plateau (e.g., Q. Y. Liu et al., 2014). The height of the topography on this boundary is kept constant throughout the model evolution. Using a fixed-height boundary condition is analogous to assuming that the central Tibetan plateau has been at its present elevation throughout the development of high topography in south-east Tibet. This simple assumption allows us to isolate the effects of lateral variations in lower-crustal strength in south-east Tibet, and is consistent with palaeoaltimetric data, which suggest that the central plateau has been high since at least the Eocene (e.g., Rowley & Currie, 2006). We assume zero deviatoric stress normal to this influx boundary ($\sigma'_{yy} = 0$), equivalent to a reservoir of high material at the edge of the model domain (i.e., the central Tibetan Plateau), which can supply fluid to the current at the same rate at which fluid moves away from the boundary (Figure 4, Appendix A; Reynolds et al., 2015). We set the velocity parallel to this boundary to zero ($u = 0$ on $y = 0$), motivated by the small velocity component parallel to the NW boundary of Figure 3. The starting topography within the model domain adjacent to this influx boundary has a constant slope in the y direction (Figure 4); its gradient does not affect the model results after the first few timesteps.

At the 'southern' end of the domain as shown in Figure 4 ($y = y_{max}$), and beyond the basins ($y > y_b$), we assume that there is an external reservoir of 40 km thick crust, which does not deform in response to the evolution of topography inside the model domain. We set the derivatives of the horizontal velocities in the direction perpendicular to these boundaries to zero (i.e., $\frac{\partial v}{\partial y} = \frac{\partial u}{\partial y} = 0$ on $y = y_{max}$, and $\frac{\partial u}{\partial x} = \frac{\partial v}{\partial x} = 0$ on $x = 0$ and $x = x_{max}$). These conditions correspond to zero deviatoric normal stress acting perpendicular to these boundaries, and boundary-parallel velocities not contributing to the shear stress on these boundaries. These boundary conditions are equivalent to there being no deviatoric stresses being imposed on the model domain by the material outside it, and are consistent with the lack of significant faulting, low earthquake- and GPS-derived strain rates, and uniform, ∼35–40 km crustal thicknesses (X. Xu et al., 2013) outside the region of south-east Tibet which corresponds to our model domain (Figure 3).

Along $x = 0$ and $x = x_{max}$ we use a reflection boundary condition up to the end of the basins ($y < y_b$). This is equivalent to assuming that mountains also exist to either side of the model domain, and are behaving in the same manner in these regions; analogous to high topography existing to the north of the Sichuan Basin and the Central Lowlands of Myanmar.

4. Results & Comparison to South East Tibet

We initially use symmetric models (i.e., where the two basins with strong lower crust have the same size and are the same distance from the influx boundary) to investigate the effects of changing basal thickness and interbasin width (defined in Figure 4) on the evolution of topography. Figure 5 shows the results of a model with symmetric basins of radius 450 km (gray semi-circles, Figure 5c, equivalent to an interbasin width of 600 km), and basal thickness 15 km. Times referred to are since the start of the model and elevations are given relative to the surface of 40 km-thick, isostatically compensated crust. As discussed in Section 3, the velocity and, therefore, the rate of topographic evolution, are expected to scale linearly with the viscosity. We therefore expect that the topography after 50 Myr of model evolution with a viscosity of 10^{22} Pas (as shown in Figure 5a) would correspond to that after 5 Myr for a viscosity of 10^{21} Pas.

Regions with a stress-free base develop gentle topographic gradients (<0.004, in contrast to gradients of ∼0.02 on the margins of the basin regions, which are discussed below). Deformation in these regions is effectively by pure shear of vertical planes; relatively gentle topographic gradients result from the quasi-depth-independent horizontal velocities. Similar, gentle topographic gradients are also a feature of thin-viscous-sheet models (England & McKenzie, 1982, 1983, even where these models use high stress-exponents; Section 3.1), which have the same, stress-free, basal boundary condition. The topographic gradients in the stress-free regions are very similar in magnitude to the south-eastwards topographic gradients in the high region between the Sichuan Basin and the Central Lowlands of Myanmar (compare Figures 6h and 6f—the topographic profile location is shown in Figure 2a). We expect these gradients to be partially controlled by the location of the model boundaries which, as discussed in Section 3.3, are consistent with the deformation and crustal thicknesses in south-east Tibet.
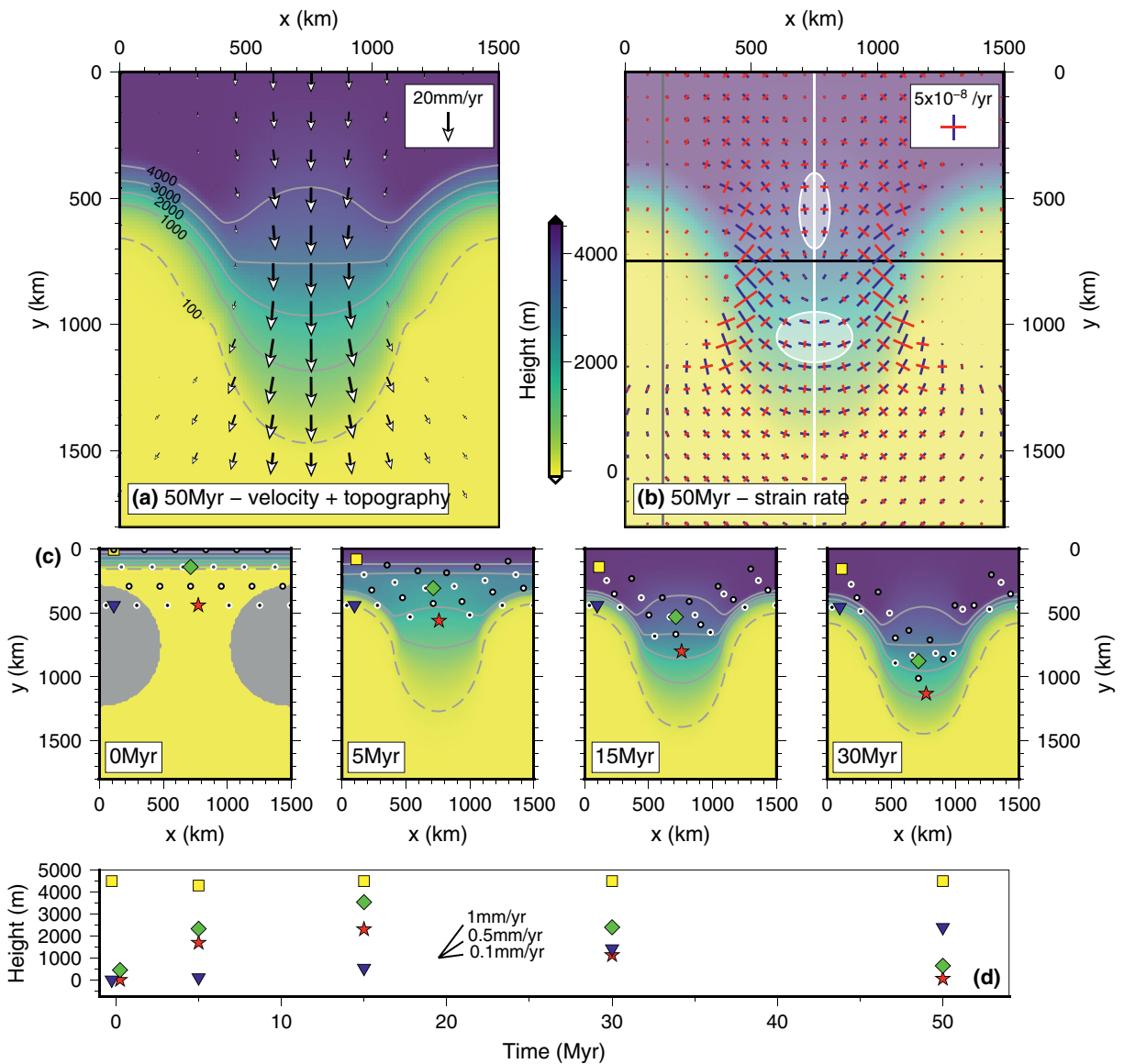
Figure 5. Modeling results for a symmetric model (both basins have the same size and location in *y*) with 450 km-radius basins (gray semicircles at 0 Myr in c) with a 15 km-thick rigid base. The influx boundary (left-hand side in Figure 4) is at the top of each panel. (a) topography and velocities after 50 Myr for a fluid with a viscosity of 10^{22} Pas. Topography is plotted relative to the surface of 40 km-thick, isostatically compensated crust and contoured at 100 m (dashed line), 1,000, 2,000, 3,000, and 4,000 m. (b) principal axes of the surface horizontal strain-rate tensor after 50 Myr. Blue bars are extensional, red bars are compressional. Gray, white and black lines show locations of profiles in Figures 6c and 6d and 7c respectively. White ellipses show the two regions where extensional strain rates are ∼2–5 times greater than compressional strain rates, discussed in Section 5. (c) Evolution of topography through time. Dots show large-scale lateral transport of particles moving with the surface of the current and can be viewed as analogous to the motion of near-surface carbonates used for palaeoaltimetry (Section 3.2). (d) shows the elevation history of the shaped particles in (c) Since the particles are advected with the current their elevation can decrease as well as increase.

In contrast to regions with a stress-free base, steep topographic gradients develop in the basin regions, suggesting that steep topography can form as a result of mountain ranges overriding rigid lower crust. The development of very different topographic gradients in regions with and without a rigid base (compare Figures 6a, 6c, and 6e to Figures 6b, 6d, and 6f), therefore, shows the first-order control exerted by the basin regions on the shape of the topography. These different topographic gradients are consistent with previous work showing that flow over a rigid base results in steeper gradients than flow over a stress-free base (e.g., McKenzie et al., 2000).
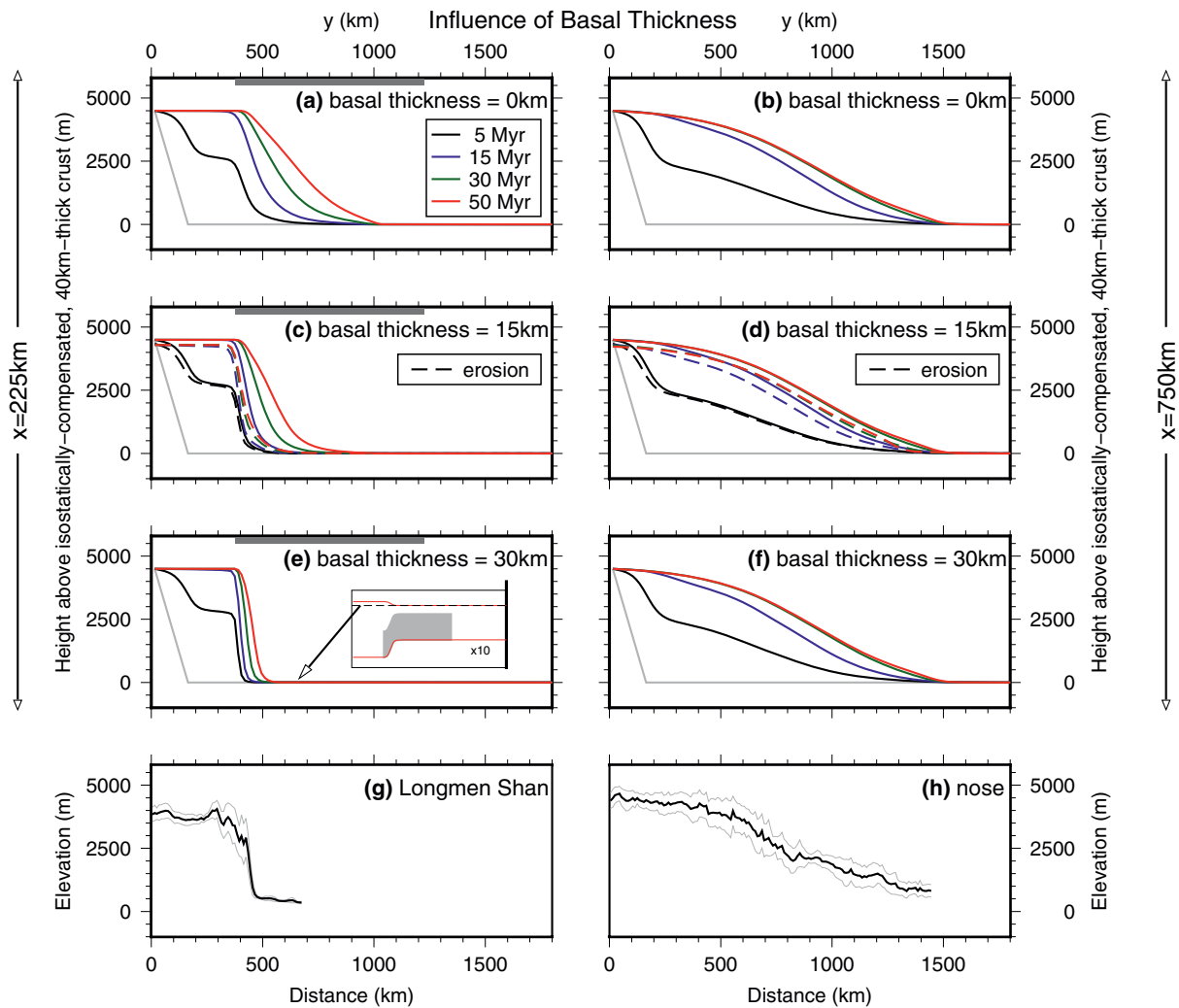
Figure 6. Effect of changing the basal thickness of the rigid basin (analogous to the thickness of undeforming lower crust) on the propagation of topography. The locations of these profiles are shown in Figure 5b. The lateral extent of the basin which has a rigid basal thickness is indicated by the gray bars in (a), (c), and (e)). (a), (c), and (e) show profiles through the basin (gray line in Figure 5b) for basal thicknesses of 0 km (rigid base), 15 and 30 km respectively. (b), (d), and (f) show profiles through the interbasin (stress-free base) region (white line in Figure 5b) for basal thicknesses of 0 km (rigid base), 15 and 30 km respectively. The basal thickness has no significant effect on the development of topography in the regions with stress-free base. Elevations are relative to the surface of 40 km-thick, isostatically compensated crust. Inset in (e) shows the full thickness of the current (10x vertical exaggeration) to demonstrate how topography in this figure relates to full model. Gray region is the rigid basin. Dashed lines in (c) and (d) show the effect of erosion with $\kappa = 4$ mm yr^{-1} in Equation 1. (c) and (d) are profiles through the same model shown in Figure 5. (g) and (h) show topographic profiles and standard deviation across the Longmen Shan and between the Sichuan Basin and Central Lowlands of Myanmar respectively (profile locations shown in Figure 2a), demonstrating the similarity of topographic gradients in south-east Tibet to those resulting from our model.

The topography also propagates more slowly in the basin regions than in the region between them (compare Figures 6c and 6d). Where flow occurs over a rigid base, the velocity depends on the square of the flow depth (Huppert, 1982). Increasing the basal thickness (analogous to having a thicker rigid lower crust or a thinner overlying layer of deformable rock) therefore, reduces the distance which the current propagates into the basin in a given time, and also results in steeper topographic profiles where the flow overrides the basin. This effect is demonstrated by Figure 6, which shows profiles through models with the same basin locations as in Figure 5, but with varying basal thicknesses. Figures 6a–6f have basal thicknesses of 0 km (only the base is rigid), 15 km and 30 km respectively. A proportionally thicker rigid region (e.g., Figure 6e) means that the current is flowing into a thinner fluid layer, so tends to develop a sharper nose, as shown by McKenzie et al. (2000). The topographic gradients across the Longmen Shan (Figure 6g) are very similar to those in our model for a basal thickness of 30 km (corresponding to 10 km initial thickness of deformable

Effect of Inter-Basin Width
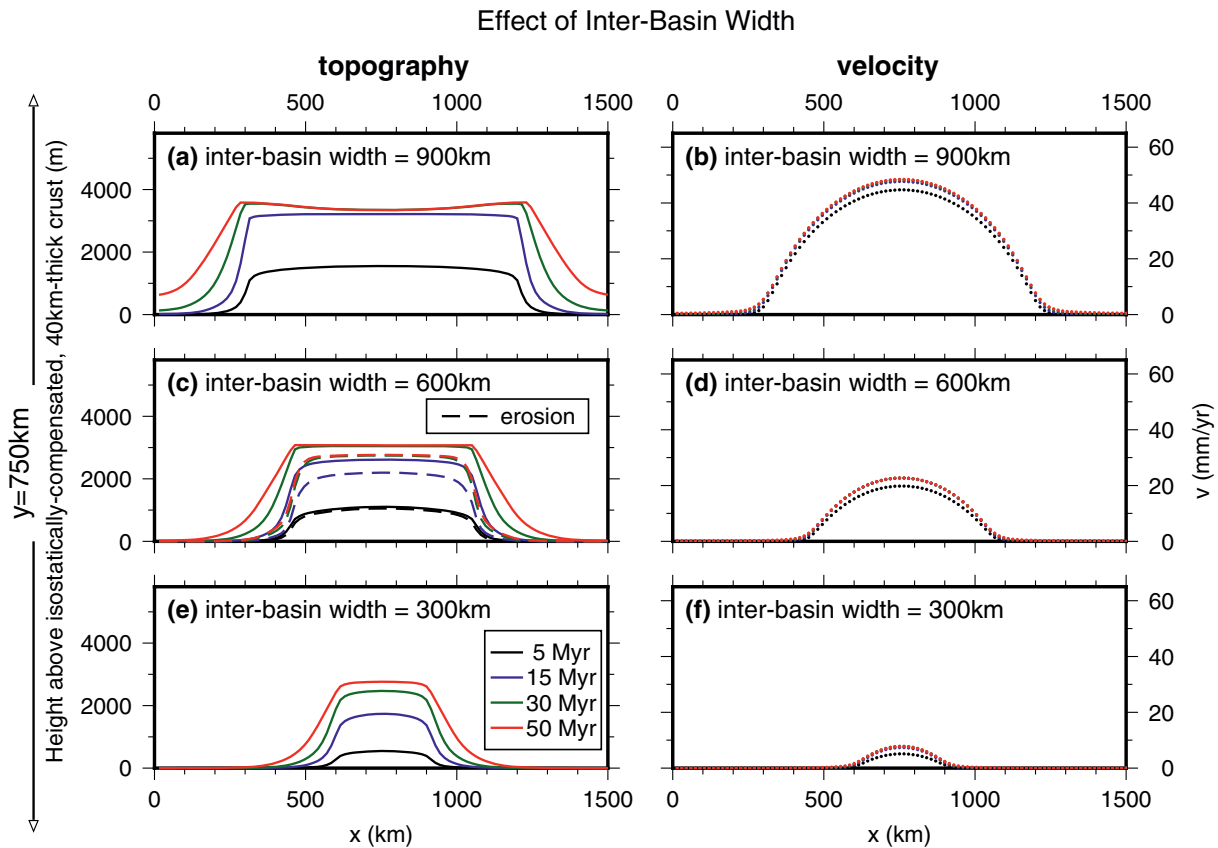
Figure 7. Effect of changing the distance between basins (interbasin width, Figure 4). In each case profiles are taken at the center of the semi-circular regions (black line in Figure 5b shows location of (c) and (d)), which have a basal thickness of 15 km. Elevations are relative to the surface of 40 km-thick, isostatically compensated crust. (a) and (b) 900 km interbasin width. (a) shows the evolution of topography through time. The slight saddle arises because of thinning due to rapid velocities in the center of the interbasin region. (b) the velocity perpendicular to the profile (v in Figure 4) after 50 Myr. (c) and (d) as for (a) and (b) but for an interbasin width of 600 km. Note that (c) and (d) are profiles through the same model as Figures 5, 6c, and 6d, with basin radius 450 km, interbasin width 600 km and basal thickness 15 km. Dashed lines show the effects of erosion with $\kappa = 4$ mm yr^{-1} in Equation 1. (e) and (f) as for (a) and (b) but for an interbasin width of 300 km.

rock in the basin regions). This basal thickness is consistent with ~10 km of sediment overlying Paleoproterozoic basement in the Sichuan Basin (Hubbard & Shaw, 2009).

Erosion also leads to steeper topographic gradients, and hinders current propagation in the basins. The dashed lines in Figures 6c and 6d show the results of eroding the topography with $\kappa = 4$ mm yr^{-1} in Equation 1. The erosive term we use is proportional to gradient (Section 3), meaning that the steep slopes in the basins are affected more than gentle slopes in the interbasin region (compare dashed lines in Figures 6c and 6d). With $\kappa = 4$ mm yr^{-1} the topography is quasi-stationary on the basin margins between 15 and 50 Myr (dashed blue and red lines in Figure 6c), demonstrating that erosion can stop the propagation of topography in these regions (equivalent to the suggestion of Koons, 1989, for the South Island of New Zealand), but not in the region of fast flow between the basins. The similar position of the present-day Longmen Shan and the Paleogene deformation front adjacent to the Sichuan Basin (derived from stratigraphic thicknesses of foreland basin sediments; Richardson et al., 2008) could, therefore, result from erosion acting on topography which would otherwise be propagating over the basin. Such an effect is possible because of the slow propagation of topography over rigid lower crust.

The distance between basins controls the velocity of the current in the region between them. Figure 7 shows the topographic and velocity profiles resulting from different interbasin widths, with constant basal thickness (15 km). Greater interbasin widths result in faster velocities perpendicular to the profile (v, Figures 7b, 7d, and 7f). Flow in the interbasin region is dominated by simple shear of horizontal planes—similar to that

between two rigid walls (as suggested by Copley & McKenzie, 2007), with maximum velocity proportional to width squared. The width of the rapidly deforming region between the Sichuan Basin and the Central Lowlands of Myanmar is ∼500 km. Observed GPS velocities relative to Eurasia in the center of this region are ∼20 mm yr^{-1}. Interbasin velocities in our model are similar to these GPS velocities for an interbasin width of 600 km, which suggests that the viscosity we use for our modeling (10^{22} Pas) is reasonable.

As discussed in Section 3.2, our models do not include flexural support of the topography. If we did include flexural support we would not expect to see qualitatively different topography, because the wavelengths associated with such support are small in comparison to the scale of our model. Viscous models of the crust, such as the one we use here, implicitly investigate long wavelength deformation, at scales longer than individual faults (Figure 3, England & McKenzie, 1982, 1983). Gravity anomalies demonstrate flexural effects in south-east Tibet acting on wavelengths less than ∼50 km (Fielding & McKenzie, 2012), and isostatic compensation throughout the region of high topography (Fielding & McKenzie, 2012; Jordan & Watts, 2005). Specifically, Fielding and McKenzie (2012) found a lower bound on the elastic thickness of the Sichuan Basin of 10 km (although this value is poorly constrained since the basin is too small for the full flexural wavelength to be measured) and an elastic thickness of 7 km for the adjacent high topography. Flexure may provide local support to the topography where it overthrusts the Sichuan Basin (in our model, over the horizontally rigid basin). The topographic gradient in this region of our model, therefore, represents an end-member in which the rigid (zero horizontal velocity) base is free to move vertically. The other end-member, in which the base cannot move vertically in response to being loaded, also leads to steep fronts (Huppert, 1982). The rigid nature of the basal boundary (i.e., the no-slip condition on the base of the fluid) controls the shape of the topography, rather than whether or not this boundary is able to deform vertically (McKenzie et al., 2000). Ball et al. (2019) demonstrated that flexural effects are primarily important near the nose of a viscous current, but that such currents over a flexed base can still form steep topographic gradients provided the base of the current has a no-slip boundary condition. The difference in basal boundaries conditions, and the depth of deformable rock, therefore, provide a first-order explanation for contrasting topographic gradients in south-east Tibet, even if our models do not capture the precise, short-wavelength details of flexural effects on the topography.

The elevation histories of particles we track at the surface of the current (Figure 5d) show that uplift rates from our model are ∼0.1–0.5 mm yr^{-1} in the center of the interbasin region (red star in Figure 5d), similar to the <0.3 mm yr^{-1} uplift rates derived from palaeoaltimetry (Section 2, Figure 2). The highest uplift rates in our model (∼0.5 mm yr^{-1}, green diamond) occur within the first 10–15 Myr of model evolution for particles moving into the interbasin region. These rates and locations are similar to those in the only region (region 1, the Gonjo basin, Figure 2) where uplift rates >0.3 mm yr^{-1} have been suggested from palaeoaltimetry in South East Tibet. However, our modeling also demonstrates that the interpretation of palaeoelevation results is not straightforward. Figure 5 shows that material at the surface may be transported long distances (hundreds of kilometer over tens of millions of years for the viscosity used here). The advection of particles with the flow means that elevation histories may be complex, with particle elevations decreasing "south" (toward $y = y_{max}$) of the interbasin region as the current spreads laterally (the same effect which leads to the extensional strain rates described below). Pedogenic carbonates which are found to have been high in the late Eocene-early Miocene (Gourbet et al., 2017; Hoke et al., 2014; S. Li et al., 2015) could have been deposited at similar latitudes to samples from the Longmen Shan, which were at their present elevation in the late Miocene (Q. Xu et al., 2016).

By considering the principal axes of the horizontal strain-rate tensor at the surface of our model (Figure 5b) as analogous to the strain rate in the brittle crust (Houseman & England, 1986), we can draw comparisons between our model and the geodetic and seismic strain rates in south-east Tibet. The largest strain-rates in both our model and in south-east Tibet are associated with shear at the basin margins. Strain rates equivalent to left-lateral shear adjacent to Basin E (Figure 4), and right-lateral shear adjacent to Basin W (Figure 4) are analogous to left-lateral slip on the Xianshuihe Fault and right-lateral slip on the Nuijiang and Sagaing Faults (and adjacent, rotating, left-lateral faults) respectively.

Where steep topography forms along the "northern" edges of the basin, the principal compressional axes of the horizontal strain rate tensor are approximately perpendicular to the basin margins. These compressional strain rates are small in comparison to the shear strain rates where the flow is subparallel to the basin
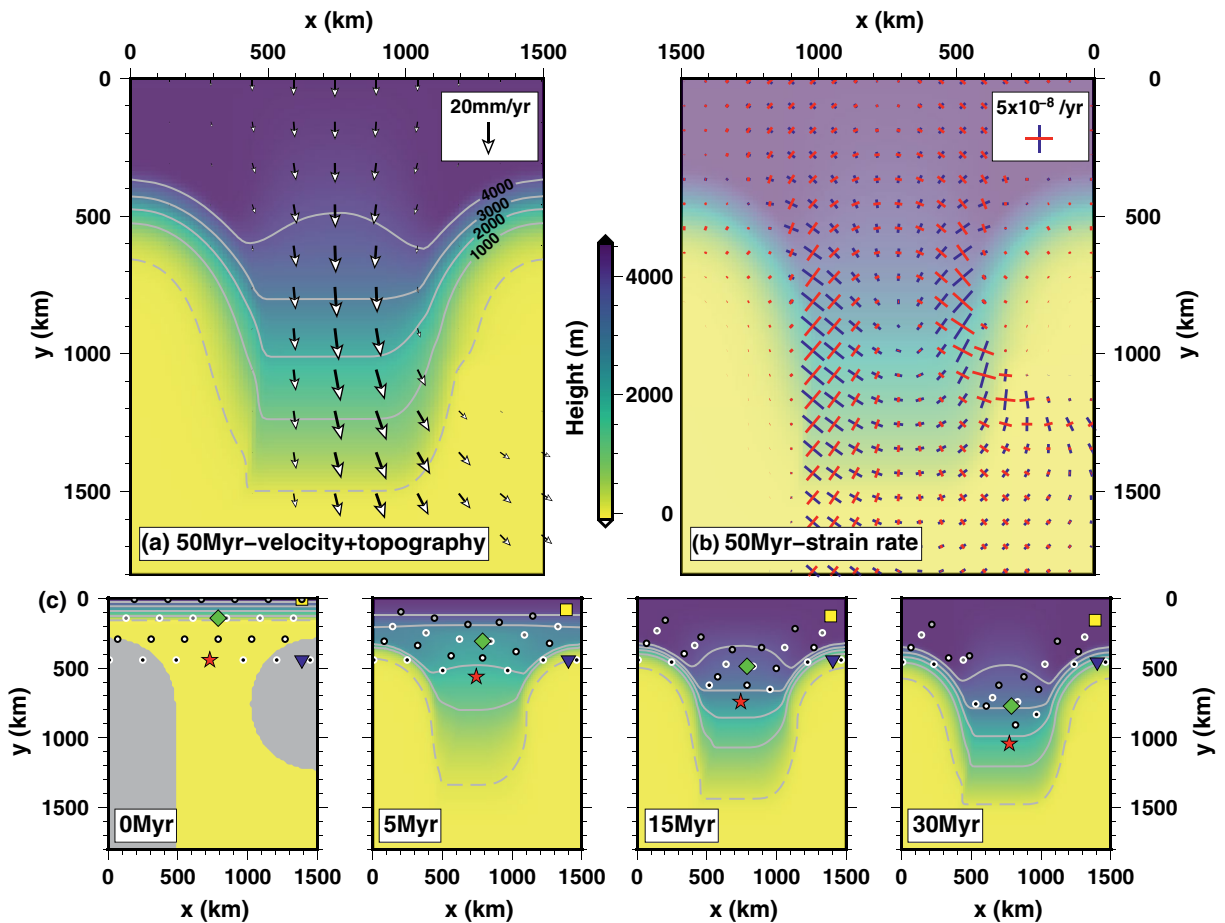
Figure 8. Modeling results for an asymmetric model set-up with 15 km basal thickness in the regions shown in gray in the 0 Myr panel of (c). Panels are as for Figure 5. Note the greater "southward" extent of shear adjacent to the extended basin.

margins. In the context of south-east Tibet, this suggests that the steep topography and low shortening rates across the Longmen Shan could result from flow of weaker material over the rigid lower crust of the Sichuan Basin (Copley, 2008; Fielding & McKenzie, 2012), without a low-viscosity, lower-crustal channel.

The principal axes of the horizontal strain-rate tensor at the surface of our models show two extension-dominated regions (red ellipses in Figure 5b), with similar locations and orientations to the normal faulting in south-east Tibet (red ellipses and focal mechanisms in Figure 1b). The extensional strain rates in these parts of our model are ~2–5 times larger than the compressional strain rates, so these regions are equivalent to mixed strike-slip and normal faulting, with normal faulting dominating. Extension in the y direction "north" of the basins (top white ellipse in Figure 5b) is comparable to the northern group of normal faults in Figure 1, which accommodate extension parallel to the topographic gradient (striking perpendicular to both topographic gradients and GPS velocities relative to Eurasia, Figure 3). Our modeling suggests that this extension may result from a velocity increase where the topography flows through the interbasin region. The second region of extension occurs where fluid spreads out laterally to the "south" of the basins; increasing the surface area of the current. This extension perpendicular to topographic gradients is shown by the bottom white ellipse in Figure 5b. The southern group of normal faults shown in Figure 1 also accommodate extension perpendicular to the topographic gradients.

Figure 8 shows the results of changing the shape of one of the basins to be more similar to that of the Central Lowlands of Myanmar. The region of shear which develops adjacent to this basin extends further "south" than that adjacent to a semi-circular basin. We expect that this larger region of shear develops because the flow is approximately parallel to the change in basal boundary condition over a longer distance
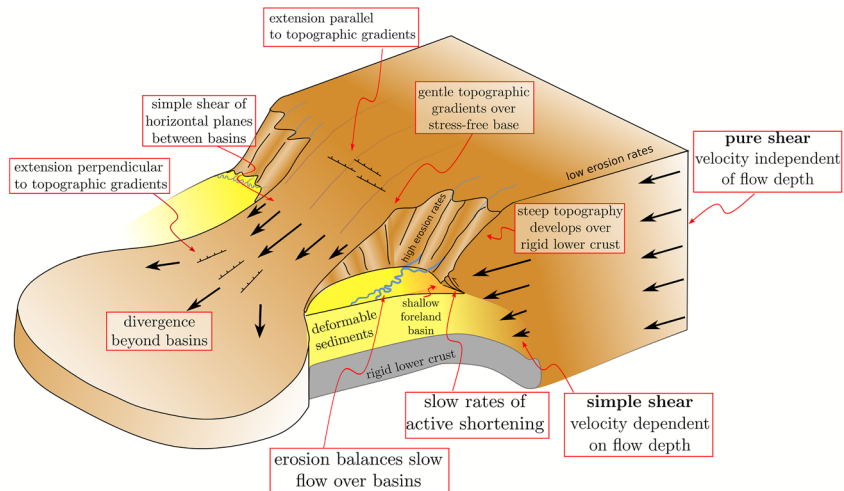
Figure 9. Cartoon showing effects of a rigid region on the development of topography. Steep topographic gradients develop above the region of rigid lower crust because of the dependence of velocity on flow depth. The compressional strain rates associated with growth of this steep topography are much less than the shear strain rates between basins. Regions with a stress-free base (without strong lower crust) deform by pure shear of vertical planes, which results in gentle topographic gradients. Between two rigid regions flow is dominated by simple shear of horizontal planes, similar to flow in a pipe. Beyond the basins the flow can spread out, leading to extension.

than when the basin is semi-circular. This region of shear is similar to the area of distributed left-lateral faulting east of the Sagaing fault (Figure 1a), which accommodates right-lateral shear through vertical-axis rotations (Copley, 2008). The lateral extent of this shear in south-east Tibet may, therefore, be controlled by the geometry of the rigid lower crust in the Central Lowlands of Myanmar.

5. Discussion

Our model, considering the effect of lateral lower crustal strength variations consistent with geophysical and geological observations, allows us to reproduce the main features of the present-day topography, strain-rate and velocity field in south-east Tibet, and uplift rates from palaeoaltimetry. These results demonstrate that lateral strength contrasts, in the form of regions of rigid lower crust, provide a first-order control on the temporal evolution of mountain ranges (Figure 9). Below we discuss our key findings and their application to mountain ranges in general.

In our model, which has mechanically coupled upper and lower crust, surface uplift rates are $<\sim 0.5$ mm yr^{-1}. These gradual uplift rates are consistent with palaeoaltimetry results in south-east Tibet, suggesting that no low-viscosity, lower-crustal channel is required to explain the evolution of topography in this region. However, our modeling also suggests a potential caveat in the interpretation of paleoaltimetry results. Particle tracking in our models shows that material at the surface where the crust flows over a stress-free base may be transported long distances (hundreds of kilometers over millions of years for the viscosity used here). Calculated palaeoelevations, therefore, estimate the palaeoelevation of the place where the sample was deposited, rather than the palaeoelevation of its present-day location. Accounting for this lateral transport is also important for converting the oxygen-isotope composition of carbonates to palaeoelevation, potentially requiring greater continentality corrections.

Our modeling demonstrates that differences in basal boundary condition, analogous to the presence or absence of strong lower crust, can lead to the development of contrasting topographic gradients. In particular, steep gradients arise naturally from flow over a rigid (no-slip) base. The present-day, compressional strain rates perpendicular to these steep margins are small in comparison to the horizontal shear strain rates where deformation is parallel to the basin margins in both our model (Figures 5 and 8), and in south-east Tibet (Figures 1 and 3, Shen et al., 2005; Zheng et al., 2017). This combination, of steep-fronted topography

and low compressional strain rates, is a feature of other parts of the India-Eurasia collision. Steep topographic gradients on the northern margin of the Tibetan Plateau, adjacent to the Tarim basin (∼3 km over 50 km), and the low rate of shortening (0–3 mm yr^{-1}, e.g., Zheng et al., 2017) across the basin margin, are similar to those in the Longmen Shan. Increasing Moho depths from north to south across the margin (Wittlinger et al., 2004), and the flexural signal seen in free-air gravity anomalies (e.g., McKenzie et al., 2019), suggests that the western edge of the Tarim Basin may underthrust the western Kunlun ranges, which would provide a rigid base to the flow of crustal material from northern Tibet, in a similar manner to the Sichuan Basin in south-east Tibet. The temporal evolution of topography adjacent to the Tarim Basin may, therefore, also be controlled by the lateral strength contrast between rigid lower crust in the Tarim Basin and lower viscosity crust in Tibet. The motion of southern Tibet over rigid India is likely to represent the same effect. However, the rates of motion in southern Tibet are more rapid than in northern Tibet, perhaps due to differences in the thicknesses, temperatures, or compositions of the crust in India and the Tarim basin (McKenzie et al., 2019).

More generally, the control on topographic evolution provided by lateral strength contrasts, particularly the low rates of propagation of topography into regions with rigid lower crust (Figures 6 and 9), suggests an explanation for the correlation of cratonic regions with steep edges of mountain belts (including the Atlas mountains, the Caucasus, and older orogenies such as the Appalachians in North America) noted by McKenzie and Priestley (2008). Cratonic regions are likely to have relatively strong lower crust (e.g., Jackson et al., 2008), so our results suggest that the propagation of topography into these regions will be slow in comparison to adjacent regions where the lower crust has lower viscosity.

We also find that the thickness of strong lower crust, and of deformable material (such as sediments) above it, controls the extent of mountain range propagation and the morphology of the range front. Larger thicknesses of deformable rock (fluid layer above the rigid base in our models) lead to more rapid propagation of topography over regions with strong lower crust, and to shallower topographic gradients. This result is likely to apply to mountain ranges globally. The occurrence of thin-skinned deformation of sediments above the edge of the South American craton, in the foothills of the Eastern Cordillera of the Andes (Lamb, 2000), suggests that the deformation in this region is comparable to flow over a rigid base. The foothills in the southern Bolivian Andes extend further east than those in the north, and have lower topographic gradients. This broader foothill region correlates with higher sediment thicknesses in the bounding basin (McGroder et al., 2014), similar to the current in our model propagating further over a rigid base where the deformable layer is thicker (Figures 6c and 6e). Wimpenny et al. (2018) suggested that this effect might lead to the onset of extension in the adjacent mountains. Along-strike variations in sediment thickness can also explain variations in the morphology of the Indo-Burman Ranges (Ball et al., 2019), although there mountain building is driven by the subducting plate, which advects sediment laterally, as well as by contrasts in gravitational potential energy. Ball et al. (2019) highlighted that it is the thickness of deformable sediment, rather than the total sediment thickness, which is important in controlling morphology. Although beyond the scope of this study, we expect that along-strike variations in the viscosity of the deformable rock, as well as its thickness, could lead to similar changes in morphology. In the Zagros mountains, for example, along-strike variations in the width of high topography could potentially correlate with the presence or absence of weak salt layers (Nissen et al., 2011). Similarly, the prominent curvature of the Sulaiman Ranges, and their projection beyond the general ∼north-south strike of the Pakistan range front, has been proposed to result from a package of weak sediments beneath them (Reynolds et al., 2015).

For crust in south-east Tibet, it is not clear whether ductile deformation is dominated by diffusion creep, which is Newtonian with a stress exponent of 1, or dislocation creep, which has a power-law rheology with a stress exponent greater than 1 (e.g., Stocker & Ashby, 1973). In our modeling, we have, therefore, taken the simplest approach, which is to use a Newtonian rheology with a constant viscosity. Our models show that such a rheology can produce steep topographic gradients where flow occurs over a rigid base, such as strong lower crust. In contrast, in models where depth variations in horizontal velocity are neglected, steep topographic gradients require a power-law rheology with a high stress exponent, and, even then, these gradients are much shallower than those in the Longmen Shan (Section 3.1, England & Houseman, 1986; Houseman & England, 1986; Lechmann et al., 2011). If dislocation creep does control ductile deformation, the vertically integrated strength of the lithosphere can be represented as a single power-law rheology (Sonder &

England, 1986). An interesting question, therefore, is whether the steep topographic gradients in our model would still form if we had used a power-law, rather than a Newtonian, rheology. A higher stress-exponent would tend to localize deformation in regions of high strain rate, such as immediately above the rigid lower crust in the basin regions. The second invariant of the strain rate tensor in these regions of our model is $\sim 10^{-15}\,\text{s}^{-1}$, consistent with geodetically- and geologically estimated strain rates in tectonically active regions (Fagereng & Biggs, 2019). For a viscosity of 10^{22} Pas this strain rate corresponds to a stress of ~ 10 MPa, typical of earthquake stress drops (Allmann & Shearer, 2009; Kanamori & Anderson, 1975). If the crust were to deform with a power-law rheology with a stress-exponent of 3, and assuming a strain rate in the rest of the model domain of $\sim 10^{-16}\,\text{s}^{-1}$, these strain rates would lead to a local drop in viscosity from 10^{22} Pas to $\sim 2 \times 10^{21}$ Pas, which might lubricate the base of the current. However, the flow over the rigid base would still be much slower than that with a stress-free base, and have a nonlinear dependence on the thickness of the current, meaning that we would still expect contrasting topographic gradients to develop. Mathematical studies of gravity currents composed of power-law fluids suggest that, although there may be some increase in far-field surface slope associated with such effects, flow over a rigid base nonetheless tends to produce a steep front (Gratton et al., 1999). Our result, that steep topographic gradients can form with a Newtonian rheology, therefore, suggests that steep-fronted mountain ranges do not constrain whether flow in the ductile part of the lithosphere occurs by diffusion or dislocation creep, but demonstrate the governing role of lower crustal strength in determining the topographic gradients of mountain ranges.

6. Conclusion

We have investigated the role of lateral contrasts in lower crustal strength in controlling the shape and evolution of mountain ranges. In south-east Tibet, stable-isotope palaeoaltimetry suggests that parts of the topography may have been at, or near, their present-day elevations since the late Eocene and that uplift is likely to have occurred more slowly than had previously been inferred. In combination with a simple model, these palaeoaltimetry results demonstrate that lateral strength contrasts are sufficient to explain first-order features of the deformation and topographic evolution in south-east Tibet, without invoking a low-viscosity, lower-crustal channel. Since our models of topographic evolution in the presence of lateral lower-crustal strength contrasts allow us to reproduce the main features of the present day topography, strain-rate and velocity field in south-east Tibet, we suggest that lateral strength contrasts provide a first-order control on the temporal evolution and shape of mountain ranges. Our modeling also suggests that lateral contrasts in lower crustal strength provide an explanation for the correlation between cratons and the steep gradients on the edges of some mountain ranges.

Appendix A: Time Evolution of a Viscous Current

We solve a simplified form of the Stokes' flow equations, proposed by Pattyn (2003) for glaciers. This form of the governing equations makes two main assumptions about the vertically oriented stresses, $\sigma_{nz} = \eta\left(\dfrac{\partial w}{\partial n} + \dfrac{\partial u_n}{\partial z}\right)$, where $n \in \{x, y\}$ represents either horizontal direction, based on scaling analysis (Pattyn, 2003). The first assumptions is that lateral variations of these stresses are small in comparison to the increase in lithostatic pressure with depth, such that the vertical normal stress is given by the lithostatic pressure:

$$\sigma_{zz} = P_l = \int_z^s \rho g dz'. \tag{A.1}$$

The second assumption is that the vertical derivatives $\dfrac{\partial \sigma_{nz}}{\partial z}$, can be neglected in the horizontal momentum balance, except in parts of the domain with no-slip boundary conditions (and immediately adjacent areas; Pattyn, 2003; Schmalholz et al., 2014). In these areas, vertical gradients in horizontal velocities, $\dfrac{\partial u_n}{\partial z}$, are important. The vertically oriented stresses are, therefore, simplified everywhere to $\sigma_{nz} = \eta\left(\dfrac{\partial u_n}{\partial z}\right), n \in \{x, y\}$.

These assumptions do not imply that the vertical velocities cannot vary horizontally, only that the terms $\frac{\partial w}{\partial n}$ do not dominate the balance of forces driving the flow.

We follow Pattyn in scaling the vertical dimension at each timestep (cf. his Equation 44). We then solve the resulting velocity equations at each timestep (subject to the boundary conditions discussed below and in Section 3.3) using the generalized minimum residual method (Saad & Schultz, 1986, in sparskit2).

At each timestep we first solve for the horizontal velocities, then calculate the associated evolution of the topography. From integrating the incompressibility condition, $\frac{\partial u}{\partial x} + \frac{\partial v}{\partial y} + \frac{\partial w}{\partial z} = 0$, over the layer thickness, H (Figure 4):

$$\frac{\partial H}{\partial t} = -\nabla_h \cdot (H\,\overline{u}, H\,\overline{v}), \tag{A.2}$$

where bars denote vertical averaging, and

$$\nabla_h = \left(\frac{\partial}{\partial x}, \frac{\partial}{\partial y} \right). \tag{A.3}$$

Equation A.2 can be written as a diffusion equation for the topography. This approach allows the diffusivities to be calculated on a staggered grid, preventing leapfrog instabilities in the second-order finite differences. Pattyn (2003) expressed this diffusion equation as:

$$\frac{\partial H}{\partial t} = \nabla_h \cdot \left(D_x \frac{\partial H}{\partial x}, D_y \frac{\partial H}{\partial y} \right) + \nabla_h \cdot \left(D_x \frac{\partial b}{\partial x}, D_y \frac{\partial b}{\partial y} \right), \tag{A.4}$$

(his Equation 55, where we make the derivatives explicit here for clarity), and:

$$D_x = \left| \overline{u}H \left(\frac{\partial s}{\partial x} \right)^{-1} \right|,$$

$$D_y = \left| \overline{v}H \left(\frac{\partial s}{\partial y} \right)^{-1} \right|,$$

(the modulus signs were implied but not included in Pattyn, 2003). In the glacier case, for which this method was developed, there is no prescribed relationship between the surface height, s, and bed depth, b (although $H = s - b$). However, for an Airy isostatically compensated fluid, such as the crust of south-east Tibet (e.g., Jordan & Watts, 2005), $b = -fs$ and $H = (1 + f)s$, where $f = \frac{\rho_c}{\rho_m - \rho_c}$. For standard crust and mantle densities of 2,700 kg m^{-3} and 3,300 kg m^{-3} respectively, $f = 4.5$, which is what we assume here. Substituting these relationships into Equation A.4 gives

$$\frac{\partial H}{\partial t} = \left(\frac{1}{f+1} \right) \left(\frac{\partial}{\partial x} \left(D_x \frac{\partial H}{\partial x} \right) + \frac{\partial}{\partial y} \left(D_y \frac{\partial H}{\partial y} \right) \right). \tag{A.5}$$

$D_n, n \in \{x, y\}$ becomes infinite if $\frac{\partial s}{\partial n} = 0$, but physically the topography in such regions should not propagate (i.e., $\frac{\partial H}{\partial t} = 0$, since in regions of flat topography there are no gravitational potential energy contrasts to drive the flow). In such cases, therefore, we set $D_n = 0$.

We write Equation A.5 as a sparse matrix equation using a Crank-Nicolson scheme for the finite differences, with diffusivities calculated on a staggered grid, the approach suggested by Pattyn (2003). Solving both x and y terms in the same linear system, rather than separating the components, gives better stability but means that the matrix does not have a simple form (the separated case is tridiagonal, which was the form

used by Reynolds et al., 2015). We therefore solve this sparse system using the generalized minimum residual method (Saad & Schultz, 1986).

Lateral Boundary Conditions

We use constant height boundary conditions on $y = 0$ ($H = 65$ km), where fluid enters the model domain, and "south" of the basins ($H = 40$ km). For the velocity boundary conditions on these boundaries, we set the deviatoric normal stresses perpendicular these boundaries to zero, that is, $\sigma'_{yy} = 2\eta \frac{\partial v}{\partial y} = 0$ on $y = 0, y = y_{max}$ and $\sigma'_{xx} = 2\eta \frac{\partial u}{\partial x} = 0$ on $x = 0, x = x_{max}$ for $y > y_b$ (where y_b denotes the "southern" end of the basins, Figure 4). On the "southern" boundaries we also impose no contribution to boundary-parallel shear stresses on vertical planes from boundary-parallel velocities, that is, $\frac{\partial u}{\partial y} = 0$ on $y = y_{max}$ and $\frac{\partial v}{\partial x} = 0$ on $x = 0, x = x_{max}$ for $y > y_b$. For the influx boundary ($y = 0$) we also set $u = 0$

On $x = 0, x = x_{max}$ we use reflection boundary conditions $u = 0, \frac{\partial v}{\partial x} = 0$ for $y < y_b$. We impose $u = 0$ directly, and use these conditions, along with our assumption of constant viscosity and $\frac{\partial v}{\partial x} = 0$ to simplify the governing equation for v and solve this equation in its co-ordinate transformed form.

Data Availability Statement

No data was created for this research. Palaeoaltimetry data can be found in Gourbet et al. (2017); Hoke et al. (2014); S. Li et al. (2015); Tang et al. (2017); Wu et al. (2018); Q. Xu et al. (2016). Earthquake focal mechanisms can be found in Copley (2008) (and references therein), Bai et al. (2017), Han et al. (2018, 2014), Z. Li et al. (2011), Zhang et al. (2010), the CMT catalog (Dziewonski et al., 1981; Ekström et al., 2012) and the ISC-EHB catalog (Engdahl et al., 1998; International Seismological Centre, 2016). GPS data in Figure 3 are from Zheng et al. (2017). The code used to produce the modeling results shown in Figures 5–8 can be found on Zenodo, https://doi.org/10.5281/zenodo.4090916.

References

Allmann, B. P., & Shearer, P. M. (2009). Global variations of stress drop for moderate to large earthquakes. *Journal of Geophysical Research*, *114*(1), 1–22. https://doi.org/10.1029/2008JB005821.

Artyushkov, E. V. (1973). Stresses in the lithosphere caused by crustal thickness inhomogeneities. *Journal of Geophysical Research*, *78*(32), 7675–7708.

Bai, L., Li, G., Khan, N. G., Zhao, J., & Ding, L. (2017). Focal depths and mechanisms of shallow earthquakes in the Himalayan-Tibetan region. *Gondwana Research*, *41*, 390–399.

Ball, T. V., Penney, C. E., Neufeld, J. A., & Copley, A. C. (2019). Controls on the geometry and evolution of thin-skinned fold-thrust belts, and applications to the Makran accretionary prism and Indo–Burman Ranges. *Geophysical Journal International*, *218*(1), 247–267.

Beaumont, C., Jamieson, R. A., Nguyen, M. H., & Lee, B. (2001). Himalayan tectonics explained by extrusion of a low-viscosity crustal channel coupled to focused surface denudation. *Nature*, *414*(6865), 738–742.

Bischoff, S., & Flesch, L. (2019). Impact of lithospheric strength distribution on India-Eurasia deformation from 3-D geodynamic models. *Journal of Geophysical Research: Solid Earth*, *124*(1), 1084–1105. https://doi.org/10.1029/2018JB015704.

Burchfiel, B. C., Royden, L. H., van der Hilst, R. D., Hager, B. H., Chen, Z., King, R. W., et al. (2008). A geological and geophysical context for the Wenchuan earthquake of 12 May 2008, Sichuan, People's Republic of China. *Geological Society of America Today*, *18*(7), 4.

Burchfiel, B. C., Zhiliang, C., Yupinc, L., & Royden, L. H. (1995). Tectonics of the Longmen Shan and adjacent regions, Central China. *International Geology Review*, *37*(8), 661–735.

Bystricky, M., & Mackwell, S. (2001). Creep of dry clinopyroxene aggregates with deformation in the dislocation creep. *Journal of Geophysical Research*, *106*, 13443–13454. https://doi.org/10.1029/2001JB000333.

Chen, L., Gerya, T. V., Zhang, Z. J., Aitken, A., Li, Z. H., & Liang, X. F. (2013). Formation mechanism of steep convergent intracontinental margins: Insights from numerical modeling. *Geophysical Research Letters*, *40*(10), 2000–2005.

Chen, L., Gerya, T., Zhang, Z., Zhu, G., Duretz, T., & Jacoby, W. R. (2013). Numerical modeling of eastern Tibetan-type margin: Influences of surface processes, lithospheric structure and crustal rheology. *Gondwana Research*, *24*(3–4), 1091–1107. https://doi.org/10.1002/grl.50446.

Clark, M. K., Bush, J. W. M., & Royden, L. H. (2005). Dynamic topography produced by lower crustal flow against rheological strength heterogeneities bordering the Tibetan Plateau. *Geophysical Journal International*, *162*, 575–590.

Clark, M. K., House, M. A., Royden, L. H., Whipple, K. X., Burchfiel, B. C., Zhang, X., & Tang, W. (2005). Late Cenozoic uplift of southeastern Tibet. *Geology*, *33*(6), 525–528.

Clark, M. K., & Royden, L. H. (2000). Topographic ooze: Building the eastern margin of Tibet by lower crustal flow. *Geology*, *28*(8), 703.

Clark, M. K., Royden, L. H., Whipple, K. X., Burchfiel, B. C., Zhang, X., & Tang, W. (2006). Use of a regional, relict landscape to measure vertical deformation of the eastern Tibetan Plateau. *Journal of Geophysical Research*, *111*, F03002. https://doi.org/10.1029/2005JF000294

Clark, M. K., Schoenbohm, L. M., Royden, L. H., Whipple, K. X., Burchfiel, B. C., Zhang, X., et al. (2004). Surface uplift, tectonics, and erosion of eastern Tibet from large-scale drainage patterns. *Tectonics*, *23*, TC1006. https://doi.org/10.1029/2002TC001402

Cook, K. L., & Royden, L. H. (2008). The role of crustal strength variations in shaping orogenic plateaus, with application to Tibet. *Journal of Geophysical Research*, *113*(8), 1–18. https://doi.org/10.1029/2007JB005457

Copley, A. (2008). Kinematics and dynamics of the southeastern margin of the Tibetan Plateau. *Geophysical Journal International*, *174*, 1081–1100.

Copley, A., Avouac, J. P., & Royer, J. Y. (2010). India-Asia collision and the Cenozoic slowdown of the Indian plate: Implications for the forces driving plate motions. *Journal of Geophysical Research*, *115*(3), 1–14. https://doi.org/10.1029/2009JB006634

Copley, A., & McKenzie, D. (2007). Models of crustal flow in the India-Asia collision zone. *Geophysical Journal International*, *169*, 683–698.

Culling, W. E. H. (1960). Analytical theory of erosion. *The Journal of Geology*, *68*(3), 336–344.

Dalmayrac, B., & Molnar, P. (1981). Parallel thrust and normal faulting in Peru and constraints on the state of stress. *Earth and Planetary Science Letters*, *55*, 473–481.

Dayem, K. E., Houseman, G. A., & Molnar, P. (2009). Localization of shear along a lithospheric strength discontinuity: Application of a continuous deformation model to the boundary between Tibet and the Tarim Basin. *Tectonics*, *28*(3), 1–15.

Dayem, K. E., Molnar, P., Clark, M. K., & Houseman, G. A. (2009). Far-field lithospheric deformation in Tibet during continental collision. *Tectonics*, *28*(6), 1–9. https://doi.org/10.1029/2008TC002344

Dziewonski, A. M., Chou, T., & Woodhouse, J. H. (1981). Determination of earthquake source parameters from waveform data for studies of global and regional seismicity. *Journal of Geophysical Research*, *86*(B4), 2825–2852.

Ekström, G., Nettles, M., & Dziewoński, A. M. (2012). The global CMT project 2004-2010: Centroid-moment tensors for 13,017 earthquakes. *Physics of the Earth and Planetary Interiors*, *200–201*, 1–9.

Engdahl, E. R., van der Hilst, R., & Buland, R. (1998). Global teleseismic earthquake relocation with improved travel times and procedures for depth determination. *Bulletin of the Seismological Society of America*, *88*(3), 722–743.

England, P., & Houseman, G. (1985). Role of lithospheric strength heterogeneities in the tectonics of Tibet and neighboring regions. *Nature*, *315*, 297–301.

England, P., & Houseman, G. (1986). Finite strain calculations of continental deformation: 2. Comparison with the India-Asia collision zone. *Journal of Geophysical Research*, *91*(B3), 3664–3676.

England, P., & McKenzie, D. (1982). A thin viscous sheet model for continental deformation. *Geophysical Journal International*, *70*, 295–321.

England, P., & McKenzie, D. (1983). Correction to: A thin viscous sheet model for continental deformation. *Geophysical Journal of the Royal Astronomical Society*, *73*, 523–532.

Fagereng, Å., & Biggs, J. (2019). New perspectives on 'geological strain rates' calculated from both naturally deformed and actively deforming rocks. *Journal of Structural Geology*, *125*(2018), 100–110.

Fielding, E. J., & McKenzie, D. (2012). Lithospheric flexure in the Sichuan basin and Longmen Shan at the eastern edge of Tibet. *Geophysical Research Letters*, *39*, L09311. https://doi.org/10.1029/2012GL051680

Flesch, L., Bendick, R., & Bischoff, S. (2018). Limitations on inferring 3D Architecture and dynamics from surface velocities in the India-Eurasia collision zone. *Geophysical Research Letters*, *45*, 1379–1386. https://doi.org/10.1002/2017GL076503

Flesch, L. M., Haines, J. A., & Holt, W. E. (2001). Dynamics of the India-Eurasia shortening. *Journal of Geophysical Research*, *106*(B8), 16435–16460.

Gourbet, L., Hervé, P., Paquette, J.-L., Sorrel, P., Maheo, G., Wang, G., et al. (2017). Reappraisal of the Jianchuan Cenozoic basin stratigraphy and its implications on the SE Tibetan plateau evolution. *Tectonophysics*, *700–701*, 162–179.

Gratton, J., Minotti, F., & Mahajan, S. M. (1999). Theory of creeping gravity currents of a non-Newtonian liquid. *Physical Review E: Statistical Physics, Plasmas, Fluids, and Related Interdisciplinary Topics*, *60*(6), 6960–6967.

Han, L., Cheng, J., An, Y., Fang, L., Jiang, C., Chen, B., et al. (2018). Preliminary report on the 8 August 2017 Ms 7.0 Jiuzhaigou, Sichuan, China, earthquake. *Seismological Research Letters*, *89*(2A), 557–569.

Han, L., Zeng, X., Jiang, C., Ni, S., Zhang, H., & Long, F. (2014). Focal mechanisms of the 2013 Mw 6.6 Lushan, China earthquake and high-resolution aftershock relocations. *Seismological Research Letters*, *85*(1), 8–14.

Hirth, G., & Kohlstedt, D. (2003). Rheology of the upper mantle and the mantle wedge: A view from the experimentalists. *Geophysical Monograph Series*, *138*, 83–105.

Hoke, G. D. (2018). Geochronology transforms our view of how Tibet's southeast margin evolved. *Geology*, *46*(1), 95–96.

Hoke, G. D., Liu-Zeng, J., Hren, M. T., Wissink, G. K., & Garzione, C. N. (2014). Stable isotopes reveal high southeast Tibetan Plateau margin since the Paleogene. *Earth and Planetary Science Letters*, *394*, 270–278.

Holmes, A. (1965). *The principles of physical geology*. Edinburgh: Nelson.

Houseman, G., & England, P. (1986). Finite strain calculations of continental deformation. 1. Method and general results for convergence zones. *Journal of Geophysical Research*, *91*(B3), 3651–3663.

Hren, M. T., Bookhagen, B., Blisniuk, P. M., Booth, A. L., & Chamberlain, C. P. (2009). δ18O and δD of streamwaters across the Himalaya and Tibetan Plateau: Implications for moisture sources and paleoelevation reconstructions. *Earth and Planetary Science Letters*, *288*, 20–32.

Huang, M. H., Bürgmann, R., & Freed, A. M. (2014). Probing the lithospheric rheology across the eastern margin of the Tibetan Plateau. *Earth and Planetary Science Letters*, *396*, 88–96.

Hubbard, J., & Shaw, J. H. (2009). Uplift of the Longmen Shan and Tibetan plateau, and the 2008 Wenchuan (M = 7.9) earthquake. *Nature*, *458*(7235), 194–197.

Hubbard, J., Shaw, J. H., & Klinger, Y. (2010). Structural setting of the 2008 Mw7.9 Wenchuan, China, earthquake. *Bulletin of the Seismological Society of America*, *100*(5B), 2713–2735.

Huppert, H. E. (1982). The propagation of two-dimensional and axisymmetric viscous gravity currents over a rigid horizontal surface. *Journal of Fluid Mechanics*, *121*, 43–58.

International Seismological Centre. (2016). *EHB bulletin*. https://doi.org/10.31905/PY08W6S3

Jackson, J., McKenzie, D., Priestley, K., & Emmerson, B. (2008). New views on the structure and rheology of the lithosphere. *Journal of Geological Society: London.*, *165*, 453–465.

Jordan, T. A., & Watts, A. B. (2005). Gravity anomalies, flexure and the elastic thickness structure of the India-Eurasia collisional system. *Earth and Planetary Science Letters*, *236*(3–4), 732–750.

Kanamori, H., & Anderson, D. (1975). Theoretical basis of some empirical relations in seismology. *Bulletin of the Seismological Society of America*, *65*(5), 1073–1095.

Kirby, E., Reiners, P. W., Krol, M. A., Whipple, K. X., Hodges, K. V., Farley, K. A., et al. (2002). Late Cenozoic evolution of the eastern margin of the Tibetan Plateau: Inferences from 40 Ar/39 Ar and (U-Th)/He thermochronology. *Tectonics*, *21*(1), 1001–1019. https://doi.org/10.1029/2000TC001246.

Koons, P. O. (1989). The topographic evolution of collisional mountain belts: A numerical look at the Southern Alps, New Zealand. *American Journal of Science*, *289*(9), 1041–1069.

Lamb, S. (2000). Active deformation in the Bolivian Andes, South America. *Journal of Geophysical Research 105*(B11), 25627–25653.

Lebedev, S., & Nolet, G. (2003). Upper mantle beneath Southeast Asia from S velocity tomography. *Journal of Geophysical Research*, *108*(B1), 2048. https://doi.org/10.1029/2000JB000073.

Lechmann, S. M., May, D. A., Kaus, B. J., & Schmalholz, S. M. (2011). Comparing thin-sheet models with 3-D multilayer models for continental collision. *Geophysical Journal International*, *187*(1), 10–33.

Lechmann, S. M., Schmalholz, S. M., Hetényi, G., May, D. A., & Kaus, B. J. P. (2014). Quantifying the impact of mechanical layering and underthrusting on the dynamics of the modern India-Asia collisional system with 3-D numerical models. *Journal of Geophysical Research: Solid Earth*, *119*(1), 616–644. https://doi.org/10.1002/2012JB009748.

Licht, A., Botsyun, S., Littell, V., Sepulchre, P., Donnadieu, Y., Risi, C., et al. (2019). *Is Tibetan Plateau uplift more recent than we thought?* AGU Fall Meeting. https://ui.adsabs.harvard.edu/abs/2019AGUFMGP51A..05L/abstract.

Licht, A., van Cappelle, M., Abels, H. A., Ladant, J.-B., Trabucho-Alexandre, J., France-Lanord, C., et al. (2014). Asian monsoons in a late Eocene greenhouse world. *Nature*, *513*(7519), 501–506.

Li, S., Currie, B. S., Rowley, D. B., & Ingalls, M. (2015). Cenozoic paleoaltimetry of the SE margin of the Tibetan Plateau: Constraints on the tectonic evolution of the region. *Earth and Planetary Science Letters*, *432*, 415–424.

Li, Z., Elliott, J. R., Feng, W., Jackson, J. A., Parsons, B. E., & Walters, R. J. (2011). The 2010 Mw 6.8 Yushu (Qinghai, China) earthquake: Constraints provided by InSAR and body wave seismology. *Journal of Geophysical Research*, *116*, B10302. https://doi.org/10.1029/2011JB008358.

Li, S., Su, T., Spicer, R. A., Xu, C., Sherlock, S., Halton, A., et al. (2020). Oligocene deformation of the Chuandian terrane in the SE margin of the Tibetan Plateau related to the extrusion of Indochina. *Tectonics*, *39*(7), e2019TC005974. https://doi.org/10.1029/2019tc005974.

Li, C., & Van Der Hilst, R. D. (2010). Structure of the upper mantle and transition zone beneath Southeast Asia from traveltime tomography. *Journal of Geophysical Research*, *115*(7), 1–19. https://doi.org/10.1029/2009JB006882.

Liu-Zeng, J., Tapponnier, P., Gaudemer, Y., & Ding, L. (2008). Quantifying landscape differences across the Tibetan plateau: Implications for topographic relief evolution. *Journal of Geophysical Research*, *113*, F04018. https://doi.org/10.1029/2007JF000897.

Liu-Zeng, J., Zhang, J., McPhillips, D., Reiners, P., Wang, W., Pik, R., et al. (2018). Multiple episodes of fast exhumation since Cretaceous in southeast Tibet, revealed by low-temperature thermochronology. *Earth and Planetary Science Letters*, *490*, 62–76.

Liu, Q. Y., van der Hilst, R. D., Li, Y., Yao, H. J., Chen, J. H., Guo, B., et al. (2014). Eastward expansion of the Tibetan Plateau by crustal flow and strain partitioning across faults. *Nature Geoscience*, *7*, 361–365.

Liu, C. Z., Wu, F. Y., Sun, J., Chu, Z. Y., & Yu, X. H. (2013). Petrology, geochemistry and ReOs isotopes of peridotite xenoliths from Maguan, Yunnan Province: Implications for the Cenozoic mantle replacement in southwestern China. *Lithos*, *168–169*, 1–14.

Maurin, T., Masson, F., Rangin, C., Min, U. T., & Collard, P. (2010). First global positioning system results in northern Myanmar: Constant and localized slip rate along the Sagaing fault. *Geology*, *38*(7), 591–594.

McGroder, M. F., Lease, R. O., & Pearson, D. M. (2014). Along-strike variation in structural styles and hydrocarbon occurrences, Subandean fold-and-thrust belt and inner foreland, Colombia to Argentina. *Geological Society of America Memoir*, *212*, 79–113.

McKenzie, D., Jackson, J., & Priestley, K. (2005). Thermal structure of oceanic and continental lithosphere. *Earth and Planetary Science Letters*, *233*, 337–349.

McKenzie, D., McKenzie, J., & Fairhead, D. (2019). The mechanical structure of Tibet. *Geophysical Journal International*, *217*(2), 950–969.

McKenzie, D., Nimmo, F., Jackson, J. A., Gans, P. B., & Miller, E. L. (2000). Characteristics and consequences of flow in the lower crust. *Journal of Geophysical Research*, *105*(B5), 11029–11046.

McKenzie, D., & Priestley, K. (2008). The influence of lithospheric thickness variations on continental evolution. *Lithos*, *102*, 1–11.

Medvedev, S. E., & Podladchikov, Y. Y. (1999a). New extended thin-sheet approximation for geodynamic applications–I. Model formation. *Geophysical Journal International*, *136*(3), 586–608.

Medvedev, S. E., & Podladchikov, Y. Y. (1999b). New extended thin-sheet approximation for geodynamic applications-II. Two-dimensional examples. *Geophysical Journal International*, *136*(3), 586–608.

Merle, O., & Guillier, B. (1989). The building of the central Swiss Alps: An experimental approach. *Tectonophysics*, *165*(1–4), 41–56.

Miller, K. G., Fairbanks, R. G., & Mountain, G. S. (1987). Tertiary oxygen isotope synthesis, sea level history, and continental margin erosion. *Paleoceanography*, *2*(1), 1–19.

Molnar, P., & Lyon-Caen, H. (1988). Some simple physical aspects of the support, structure, and evolution of mountain belts. *Geological Society of America Special Paper*, *218*, 179–208.

Molnar, P., & Tapponnier, P. (1978). Active tectonics of Tibet. *Journal of Geophysical Research*, *83*(B11), 5361–5375.

Nissen, E., Tatar, M., Jackson, J., & Allen, M. (2011). New views on earthquake faulting in the Zagros fold-and-thrust belt of Iran. *Geophysical Journal International*, *186*, 928–944.

Pattyn, F. (2003). A new three-dimensional higher-order thermomechanical ice sheet model: Basic sensitivity, ice stream development, and ice flow across subglacial lakes. *Journal of Geophysical Research*, *108*(B8), 1–15. https://doi.org/10.1029/2002JB002329.

Pusok, A. E., & Kaus, B. J. P. (2015). Development of topography in 3-D continental-collision models. *Geochemistry, Geophysics, Geosystems*, *16*(5), 1378–1400. https://doi.org/10.1002/2015GC005732.

Ramberg, H. (1981). The role of gravity in orogenic belts. *Geological Society: Special Publications*, *9*, 125–140.

Reynolds, K., Copley, A., & Hussain, E. (2015). Evolution and dynamics of a fold-thrust belt: The Sulaiman Range of Pakistan. *Geophysical Journal International*, *201*, 683–710.

Richardson, N. J., Densmore, A. L., Seward, D., Fowler, A., Wipf, M., Ellis, M. A., et al. (2008). Extraordinary denudation in the Sichuan Basin: Insights from low-temperature thermochronology adjacent to the eastern margin of the Tibetan Plateau. *Journal of Geophysical Research*, *113*, B04409.

Rowley, D. B., & Currie, B. S. (2006). Palaeo-altimetry of the late Eocene to Miocene Lunpola basin, central Tibet. *Nature*, *439*, 677–681.

Rowley, D. B., Pierrehumbert, R. T., & Currie, B. S. (2001). A new approach to stable isotope-based paleoaltimetry: Implications for paleo-altimetry and paleohypsometry of the High Himalaya since the late Miocene. *Earth and Planetary Science Letters*, *188*, 253–268.

Royden, L. H., Burchfiel, B. C., King, R. W., Wang, E., Chen, Z., Shen, F., & Liu, Y. (1997). Surface deformation and lower crustal flow in eastern Tibet. *Science*, *276*(5313), 788–790.

Rybacki, E., Gottschalk, M., Wirth, R., & Dresen, G. (2006). Influence of water fugacity and activation volume on the flow properties of fine-grained anorthite aggregates. *Journal of Geophysical Research*, *111*(3), B03203. https://doi.org/10.1029/2005JB003663

Saad, Y., & Schultz, M. H. (1986). GMRES: A generalized minimal residual Algorithm for solving nonsymmetric linear systems. *SIAM Journal on Scientific and Statistical Computing*, *7*(3), 856–869.

Savin, S. M. (1977). The history of the Earth's surface temperature during the past 100 million years. *Annual Review of Earth and Planetary Sciences*, *5*(1), 319–355.

Schmalholz, S. M., Medvedev, S., Lechmann, S. M., & Podladchikov, Y. (2014). Relationship between tectonic overpressure, deviatoric stress, driving force, isostasy and gravitational potential energy. *Geophysical Journal International*, *197*(2), 680–696.

Shen, Z. K., Lü, J., Wang, M., & Bürgmann, R. (2005). Contemporary crustal deformation around the southeast borderland of the Tibetan Plateau. *Journal of Geophysical Research*, *110*, B11409. https://doi.org/10.1029/2004JB003421

Sonder, L. J., & England, P. (1986). Vertical averages of rheology of the continental lithosphere: Relation to thin sheet parameters. *Earth and Planetary Science Letters*, *77*, 81–90.

Steckler, M. S., Mondal, D. R., Akhter, S. H., Seeber, L., Feng, L., Gale, J., et al. (2016). Locked and loading megathrust linked to active subduction beneath the Indo-Burman Ranges. *Nature Geoscience*, *9*, 615–618.

Stocker, R. L., & Ashby, M. F. (1973). On the rheology of the upper mantle. *Review of Geophysics*, *11*(2), 391–426.

Stork, A. L., Selby, N. D., Heyburn, R., & Searle, M. P. (2008). Accurate relative earthquake hypocenters reveal structure of the Burma subduction zone. *Bulletin of the Seismological Society of America*, *98*(6), 2815–2827.

Tang, M., Liu-Zeng, J., Hoke, G. D., Xu, Q., Wang, W., Li, Z., et al. (2017). Paleoelevation reconstruction of the Paleocene-Eocene Gonjo Basin, SE-central Tibet. *Tectonophysics*, *712–713*, 170–181.

Vilotte, J. P., Daignieres, M., Madariaga, R., & Zienkiewicz, O. C. (1984). The role of a heterogeneous inclusion during continental collision. *Physics of the Earth and Planetary Interiors*, *36*, 236–259.

Wang, E., & Burchfiel, B. C. (1997). Interpretation of Cenozoic tectonics in the right-lateral accommodation zone between the Ailao Shan shear zone and the eastern Himalayan syntaxis. *International Geology Review*, *39*(3), 191–219.

Wang, E., Kirby, E., Furlong, K. P., Van Soest, M., Xu, G., Shi, X., et al. (2012). Two-phase growth of high topography in eastern Tibet during the Cenozoic. *Nature Geoscience*, *5*, 640–645.

Wang, Y., Sieh, K., Tun, S. T., Lai, K.-Y., & Myint, T. (2014). Active tectonics and earthquake potential of the Myanmar region. *Journal of Geophysical Research: Solid Earth*, *119*, 3767–3822. https://doi.org/10.1002/2013JB010762

Wang, Y., Zhang, B., Schoenbohm, L. M., Zhang, J., Zhou, R., Hou, J., & Ai, S. (2016). Late Cenozoic tectonic evolution of the Ailao Shan-Red River fault (SE Tibet): Implications for kinematic change during plateau growth. *Tectonics*, *35*, 1969–1988. https://doi.org/10.1002/2016TC004229

Wessel, P., Smith, W. H. F., Scharroo, R., Luis, J., & Wobbe, F. (2013). Generic mapping tools: Improved version released. *EOS Transactions AGU*, *94*(45), 409–410. https://doi.org/10.1002/2013EO450001

Wimpenny, S., Copley, A., Benavente Escobar, C. L., & Aguirre, E. (2018). Extension and dynamics of the Andes inferred from the 2016 Parina (Huarichancara) earthquake. *Journal of Geophysical Research: Solid Earth*, *123*(9), 1–31. https://doi.org/10.1029/2018JB015588

Wittlinger, G., Vergne, J., Tapponnier, P., Farra, V., Poupinet, G., Jiang, M., et al. (2004). Teleseismic imaging of subducting lithosphere and Moho offsets beneath western Tibet. *Earth and Planetary Science Letters*, *221*(1–4), 117–130.

Wu, J., Zhang, K., Xu, Y., Wang, G., Garzione, C. N., Eiler, J., et al. (2018). Paleoelevations in the Jianchuan Basin of the southeastern Tibetan Plateau based on stable isotope and pollen grain analyses. *Palaeogeography, Palaeoclimatology, Palaeoecology*, *510*, 93–108.

Xiong, Z., Ding, L., Spicer, R. A., Farnsworth, A., Wang, X., Valdes, P. J., et al. (2020). The early Eocene rise of the Gonjo Basin, SE Tibet: From low desert to high forest. *Earth and Planetary Science Letters*, *543*, 116312.

Xu, X., Ding, Z., Shi, D., & Li, X. (2013). Receiver function analysis of crustal structure beneath the eastern Tibetan plateau. *Journal of Asian Earth Sciences*, *73*, 121–127.

Xu, Q., Liu, X., & Ding, L. (2016). Miocene high-elevation landscape of the eastern Tibetan Plateau. *Geochemistry, Geophysics, Geosystems*, *17*(10), 4254–4267. https://doi.org/10.1002/2016GC006437

Yang, R., Willett, S. D., & Goren, L. (2015). In situ low-relief landscape formation as a result of river network disruption. *Nature*, *520*, 526–529.

Yu, H. M., Lin, C. Y., Shi, L. B., Xu, J. D., & Chen, X. D. (2010). Characteristics and origin of mafic and ultramafic xenoliths in trachyandesite lavas from Heikongshan volcano, Tengchong, Yunnan Province, China. *Science China Earth Sciences*, *53*(9), 1295–1306.

Zachos, J., Pagani, H., Sloan, L., Thomas, E., & Billups, K. (2001). Trends, rhythms, and aberrations in global climate 65 Ma to present. *Science*, *292*(5517), 686–693.

Zhang, P.-Z., Wen, X.-Z., Shen, Z.-K., & Chen, J.-H. (2010). Oblique, high-angle, Listric-reverse faulting and associated development of strain: The Wenchuan earthquake of May 12, 2008, Sichuan, China. *Annual Review of Earth and Planetary Sciences*, *38*(1), 353–382. https://doi.org/10.1146/annurev-earth-040809-15260

Zheng, G., Wang, H., Wright, T. J., Lou, Y., Zhang, R., Zhang, W., et al. (2017). Crustal deformation in the India-Eurasia collision zone from 25 Years of GPS measurements. *Journal of Geophysical Research: Solid Earth*, *122*(11), 9290–9312. https://doi.org/10.1002/2017JB014465